FISH-LIKE LOCOMOTION USING FLEXIBLE PIEZOELECTRIC COMPOSITES FOR UNTETHERED AQUATIC ROBOTICS

A Thesis
Presented to
The Academic Faculty

by

Lejun Cen

In Partial Fulfillment
of the Requirements for the Degree
Master of Science in the
School of Mechanical Engineering

Georgia Institute of Technology
December 2012

FISH-LIKE LOCOMOTION USING FLEXIBLE PIEZOELECTRIC COMPOSITES FOR UNTETHERED AQUATIC ROBOTICS

Approved by:

Dr. Alper Erturk, Advisor
School of Mechanical Engineering
Georgia Institute of Technology

Dr. Aldo A. Ferri
School of Mechanical Engineering
Georgia Institute of Technology

Dr. Alexander Alexeev
School of Mechanical Engineering
Georgia Institute of Technology

Date Approved: [September 27th , 2012]

ACKNOWLEDGEMENTS

First of all, I would like to thank my advisor Dr. Alper Erturk for giving me the opportunity to join his lab as research assistant during these semesters. He teaches me almost hand by hand, from setting up device to analyzing data. To be honest, I learn a lot from his patient guidance throughout my time at Georgia Tech. I really appreciate his guidance and financial support. Without these, it is hard to imagine I can learn and do research in Georgia Tech.

I would also like to thank Dr. Aldo A. Ferri and Dr. Alexander Alexeev for taking the time to participate in my thesis committee. Besides, Dr. Aldo A. Ferri helped me a lot during his office hours when I took his courses of dynamics and vibration. All these knowledge are very helpful in my current research topic. During the group meeting with Dr. Alexander Alexeev and his PhD student Peter Yeh, I also got valuable suggestion and feedback for this research. I am grateful to all of them for being so nice to me. Their passion for teaching, research, and mentoring of students is inspiring.

I express my gratitude to the students in Smart Structures and Dynamical Systems Lab: Mr. Martin R. Cacan, Ms. Sihong Zhao and Mr. Algan Samur. Specifically I would like to thank Mr. Martin R. Cacan for his assistance in CAD modeling of the robotic fish sample. Sihong Zhao and Algan Samur also help me a lot in various matters, such as adjusting experiment devices and taking video for the robotic fish.

I would also like to take this opportunity to thank the students in Wave Physics Lab and Active Control Lab. They provided a lot of guidance in utilizing the devices and even lend me some of the devices, such as power source, oscilloscope, and reflected mirrors. All of these are very important for my current research.

Finally, I want to give a special thanks to my friends and family for their encouragement, especially my parents. As a second son in China, I understand that they sacrificed a lot (jobs, money, etc.) to bring me to this world. Words alone cannot fully express my appreciation to what they have done for me.

TABLE OF CONTENTS

LIST OF TABLES

LIST OF FIGURES

LIST OF SYMBOLS AND ABBREVIATIONS

BCF	Body and/or Caudal Fin
IPMC	Ionic Polymer-Metal Composites
MFC	Macro-Fiber Composite
MPF	Median or Pectoral Fins
PIV	Particle Image Velocimetry
SMA	Shape Memory Alloy
b	width of the bimorph
c	damping coefficient
C_D	drag coefficient
C_T	thrust coefficient
D	flexural rigidity of the composite cross section
F_D	drag force
h	thickness of the bimorph
j	unit imaginary number
K_0 and K_1	modified Bessel functions of the third kind
L	length of the bimorph
m	mass per length
m_s	structural mass per length
m_a	added mass per length
m_v	virtual mass per length

Re	Reynolds number
Re_L	modified Reynolds number
S	wetted surface area
T	mean thrust
U	swimming speed
$v(t)$	actuation voltage
V_0	actuation voltage amplitude
w	deflection of the reference surface in the transverse direction
α	virtual mass coefficient
β	relative peak tip displacement
$\delta(x)$	Dirac delta function
δ_p	peak tip displacement
Θ	hydrodynamic function for large amplitude vibration
θ	electromechanical coupling term in the modal coordinates
$\Omega(\mathrm{Re})$	correction function to approximate the hydrodynamic function of rectangular beam from circular cylinder
ζ_h	hydrodynamic damping ratio
ζ_s	in-air damping ratio
ϑ	electromechanical coupling term in the physical coordinates
$\phi(x)$	mass-normalized eigenfunction for a clamped-free uniform beam
$\eta(t)$	modal coordinate of the fundamental transverse vibration mode
Γ	hydrodynamic function for small amplitude vibration

$\Delta\Gamma$	correction term in the hydrodynamic function for large amplitude vibration
K	Keulegan-Carpenter number
ρ_w	mass density of water
μ	viscosity of water
τ	thrust per unit width of the bimorph
υ	kinematic viscosity of water $\left(\upsilon = \mu/\rho_w\right)$
$\omega_{n,air}$	in-air natural frequency
$\omega_{n,water}$	underwater natural frequency
ω	actuation frequency (in rad/s)

SUMMARY

It is well-known that fish achieve excellent efficiency and maneuverability, comparing with conventional propeller based marine vehicles [1]. The ability of humankind to mimic fish-like propulsion for aquatic locomotion at different geometric scales depends mainly on the availability of suitable actuators. Researchers have recently focused on developing robotic fish using smart materials, particularly Ionic Polymer-Metal Composites (IPMCs), as a compliant, noiseless, and scalable alternative to conventional motor-based propulsion systems.

Similar to IPMCs, Macro-Fiber Composite (MFC) piezoelectric actuators also offer scalability, low power consumption, and silent performance. In addition, MFCs offer strong electromechanical coupling and large dynamic stresses in bending actuation as well as actuation capability over a range of frequencies for adaptive swimming. However, to the best of our knowledge, untethered piezoelectric robotic fish (without external power supply) does not exist in the literature [2-5]. High voltage input requirement and low strain output are the two limitations of piezoelectric transduction for robotic fish development.

In this thesis, an untethered piezoelectric (MFC-based) robotic fish prototype is developed and tested in free locomotion. In order to reduce noise and power consumption, no traditional magnification components (e.g., such as gears and bearings) are employed. The untethered prototype serves to exploit the potential benefits of piezoelectric fish-like propulsion. An MFC-based flexible bimorph fin and an autonomous power system were implemented to overcome the primary limitations of piezoelectric material (low strain and high input voltage). A swimming speed of 0.3 body length per second (7.5 cm/s swimming speed for 24.3 cm body length) is achieved for a non-optimized main body–propulsor combination under moderate actuation voltage level, which is substantially larger than typical IPMC-based robotic fish

configurations recently studied in the literature. The prototype also has embedded wireless control system, which enables maneuverability using the same propulsor fin.

In addition, fish-like thrust generation using MFC piezoelectric bimorphs is investigated theoretically and experimentally. First the in-air dynamics of an MFC bimorph cantilever fin is modeled for linear bending vibrations under dynamic piezoelectric actuation. The in-air electroelastic model is extended to obtain an underwater electrohydroelastic model accounting for the hydrodynamic effects following the work by Sader and others on atomic force microscopy incorporating fluid effect [6-9]. In-air and underwater experiments are conducted for model validation and for characterizing a bimorph propulsor.

A thrust estimation model that couples the actuator dynamics and hydrodynamic effects is indispensable to optimal design and control of biomimetic robotic fish. Lighthill's slender-body theory [10-12] is used to predict the thrust output in quiescent water, in the absence of a complete theory for estimating the thrust of vibrating cantilever beams in placid environment [13]. By reducing Lighthill's mean thrust expression to the quiescent water condition, the tail tip velocity is related to mean thrust output with good accuracy.

CHAPTER 1

INTRODUCTION

1.1 Motivation

Motor-based marine propulsion systems, such as screw propellers, are power hungry, cumbersome, and noisy as compared to many aquatic animals that have been optimized through the natural selection process for millions of years. The capacity of humankind to mimic these products of evolution at different geometric scales highly depends on the availability of suitable actuators. The motivation for fish-like biomimetic locomotion ranges from underwater sensing and exploration for sustainable ecology to drug delivery and disease screening in medicine [14-16]. Recently, several types of smart materials have been utilized for robotic fish development, such as Ionic Polymer-Metal Composites (IPMCs) [17-30], Shape Memory Alloys (SMAs) [31-36], magnetostrictive thin films [37-39], among other alternatives [40-42]. In particular, the IPMC technology [17-30] has received great interest for biomimetic locomotion primarily due to its low-voltage actuation and large-amplitude deflection capabilities.

Piezoelectric materials offer strong electromechanical coupling, large power density, and their fabrication methods at different scales are well established. From the point of view of multifunctionality, the converse piezoelectric effect can be used for dynamic actuation in biomimetic locomotion at low-to-moderate frequencies, while the direct piezoelectric effect can be employed for harvesting underwater energy toward enabling self-powered swimmer-sensor platforms [43]. Similar to IPMCs, Macro-Fiber Composite (MFC) piezoelectric actuators (developed at the NASA Langley Research Center in the last decade [44] [45]) also exhibit high efficiency in size, reduced energy consumption, and noiseless performance. In addition, MFCs

offer large dynamic stresses in bending actuation as well as high performance for both low-frequency and high-frequency applications. The MFC technology employs piezoelectric fibers of rectangular cross section along with interdigitated electrodes and leverages the effective 33-mode of piezoelectricity in bending actuation [45].

To the best of our knowledge, untethered piezoelectric robotic fish does not exist in the literature [2-5]. High voltage input requirement and low strain output are the two downsides of piezoelectric transduction limiting the application of previously investigated piezoelectric structures for robotic fish development to use in free locomotion. In order to overcome the shortage of low strain in piezoelectric robotic configurations prior to the MFC technology, various magnification mechanisms were proposed by others [2-4]. However, the magnification component that is employed for creating larger vibration amplitudes might create noise and cause additional energy loss. As far as the high input voltage requirement is concerned, research groups used tethered configuration to power piezoelectric robotic fish, which restricts the free-locomotion capability [2-5].

In addition, a thrust estimation model that couples the actuator dynamics and hydrodynamic effect is essential to optimal design and control of biomimetic robotic fish. In the absence of a complete theory for estimating the thrust of a vibrating cantilever beams in placid environment [13], many IPMC-based robotic fish groups have tried different theories in thrust estimation for IPMC beam. Similarly, a thrust estimation model for piezoelectric cantilever beam will also be beneficial in the future optimization of the piezoelectric robotic fish design.

1.2 Research objective

The objective of this research is to investigate the fundamentals of fish-like propulsion using flexible piezoelectric composites in quiescent water and free swimming conditions for performance enhancement in aquatic robotics. To this end, the goals in this thesis can be summarized as follows:

- Experimental testing and modeling of electroelastic propulsor dynamics for in air and under water vibrations
- Development of a simple yet reliable experimental setup for thrust measurement under quiescent water condition
- Establishment of the relationship between the underwater dynamics (velocity response) of the propulsor and the mean thrust output
- Validation of the tip velocity and thrust relationship in quiescent water condition for different actuation voltage levels
- Investigating the dependence of mean thrust on the modified Reynolds number and extracting the hydrodynamic thrust coefficient
- Development of a compact control system for untethered swimming (free locomotion) by achieving high voltage (e.g., peak-to-peak 1000 V) oscillatory signal transmission to the piezoelectric propulsor by using simple batteries
- Introduction and validation of a simple turning mechanism by breaking the symmetry of the vibration response due to asymmetric voltage actuation

The next section presents the outline of this thesis in order to achieve the foregoing theoretical and experimental research goals.

1.3 Overview of thesis

Chapter 2 presents the background and literature reviews of smart material-based robotic fish. Significance of the current research is also discussed in this chapter. Chapter 3 provides the theoretical background for modeling and thrust estimation methods. Chapter 4 describes the experimental setup and methods for in-air and underwater velocity measurement as well as thrust measurement. Chapter 5 compares the experimental results with the theory in chapter 2 and discusses the thrust estimation results and extracts the thrust coefficient. Chapter 6 describes the design of the untethered piezoelectric robotic fish and compares the test results with other robotic fish. Finally, the last chapter discusses the conclusions and provides recommendations for future work in this field.

CHAPTER 2

BACKGROUND AND SIGNIFICANCE

2.1 Fundamentals of fish swimming modes

In 1978, Lindsey discussed different swimming modes under three types of propulsions [46]: (1) Body and/or Caudal Fin (BCF) propulsion, and propulsion mechanisms employing Median or Pectoral Fins (MPF) for (2) undulation and (3) oscillation. In BCF propulsion, the fish generates thrust by bending its body into a backward-moving propulsive wave that extends to the caudal fin while median and pectoral fins are utilized to create propulsion in MPF type. In general, MPF propulsion offers better maneuverability with low speed whereas BCF propulsion can achieve greater levels of thrust and acceleration. Since BCF propulsion has been widely employed in robotic fish research, our discussion will focus on BCF type locomotion for the swimming modes and the self-propulsion theory.

Three different modes of swimming were described by Breder in 1926: anguilliform, carangiform, and ostraciiform [47]. Later, Breder's intermediate term "carangiform" has been expanded to include other different swimming modes which may require more than one hydrodynamic model [48]. Therefore the "carangiform" type has been expanded to cover three swimming modes: "subcarangiform," "carangiform," and "thunniform". This expanded classification has been widely used by several research groups although the nomenclature has not been uniform in the literature [46]. The movement of fish body changes from undulatory to oscillatory as one moves from anguilliform to ostraciiform.

The suffix "-form" in the classification of BCF swimming modes refers to the types of movement rather than the body forms [47]. The criterion for the swimming mode classification is

based on the similarity of hydrodynamic analyses, which may be applicable to fish swimming in a similar pattern [46], depending on the type of movements (oscillatory or undulatory) employed for thrust generation [49]. Breder (1926), Bainbridge (1963), and Webb (1975) have stressed that these classifications should be considered as an essentially continuous range of swimming modes, rather than discrete sets [47]. Oscillatory movements can eventually be derived from the gradual increase of the undulation wavelength [49].

2.2 Types of smart materials used in aquatic locomotion

2.2.1 Electroactive polymers

Electroactive polymers have an outstanding ability to produce large strains, with correspondingly lower forces, due to their elastic modulus [50]. Electroactive polymers can be classified into two types: (1) electronic and (2) ionic materials.

Electronic materials: This classification scheme defines electronic electroactive polymer materials as those that exhibit coupling due to polarization-based or electrostatic mechanisms, such as irradiated *piezoelectric* film and *dielectric* elastomers. They share some similarities that the electromechanical coupling comes from electrostatic interactions such as material polarization (as in the case of a piezoelectric) or Maxwell stress.

Ionic materials: Different from those of electronic materials, ionic materials is conducting charged atoms or molecules, whereas an electronic conductor is conducting electrons. Their electromechanical coupling results from the transport of charged species within the material, which leads to charge imbalance in polymer networks. Ionic materials generally require voltages on the order of less than 5V to operate. Two popular types of polymer materials that exhibit

electromechanical coupling due to charge migration are *conducting polymers* and *ionomeric polymers*.

Within ionic materials, *conducting polymers* are a class of polymer material that exhibits electronic conduction in a manner similar to that of conductive metals. While *ionomeric materials* are based on a class of polymer known as ionomers, polymers composed of macromolecules that have a small but significant portion of ionic groups, such as Ionic Polymer Metal Composite (IPMC).

Electroactive conducting polymers can be used as actuators in robotic fish, such as polyacetylene (PA), polythiophene (PT), polyaniline (PANI) and polypyrrole (PPy). They have good conductivities as metals when doped electrochemically. Different research groups have been dedicated to the synthesis, analysis and modeling of conducting polymers since 1970 [51-54].

The electromechanical coupling in IPMC can be generated by application of an electric field, which results in the ionic species migration. Similar to other ionic materials, mechanical deformation can be induced by the application of a voltage that is generally less than 5 V. Since 1991, IPMC has been widely utilized in robotic fish by different research groups since they produce large bending motions at the expense of low actuation force under low voltage.

2.2.2 Shape memory alloys

A shape memory material has the ability to return to its predetermined shape upon an external stimulus, such as thermally activated shape memory materials and magnetically activated shape memory materials, etc. Since thermally activated ones are more popular in the recent robotic fish application, our discussion will focus on it in the later sections.

There are two interesting nonlinear phenomena in the stress-strain behavior of shape memory materials, that is, the *pseudoelastic effect* and the *shape memory effect* [50], as summarized in the following:

Pseudoelastic effect: The material exhibits a very large strain upon loading that is covered fully when the material is unloaded. A shape memory material exhibiting the pseudoelastic effect exhibits a very large hysteresis loop in the stress-strain curve. *Shape memory effect:* Martensite structures at low temperature can be recovered to austenite structures by heating the material above a critical temperature. During the shape recovery, large contractions appear in the shape memory materials, which make it useful in robotic fish fin applications.

The ability for shape memory alloys (SMA) to fully recover large strains is due to a phase transformation. When the temperature is high, SMA exists in strong and predetermined austenitic phase in a stress-free state. As the temperature decreases, the material phase transforms into soft and ductile martensite. The phase transformation between the martensitic and austenitic phases results in large mechanical strains in the shape memory alloy and induces both the shape memory effect and the pseudoelastic effect [50].

2.2.3 Piezoelectric materials

Most piezoelectric materials belong to a class of crystalline solids. The piezoelectric response of materials was discovered by the Curies, who found that some crystals can convert mechanical deformation into electricity. In 1881, the term “piezoelectricity” was proposed by W. G. Hankel. Later, a classical theory for single crystals was developed by Voigt 1890. This theory shows that, there are 32 crystal classes. 20 of them are noncentrosymmetric and can be piezoelectrically active. Piezoelectricity is the charge which accumulates in certain solid

materials (such as crystals, and certain ceramics) when a mechanical stress is applied [50, 55]. The electromechanical coupling in piezoelectric materials is very useful in the design of actuation devices.

The piezoelectric effect is a reversible process, which exhibits direct piezoelectric effect (the internal generation of electrical charge resulting from an applied mechanical force) and converse piezoelectric effect (the internal generation of a mechanical strain resulting from an applied electrical field).

The converse piezoelectric effect is applied in many actuation systems. Even though several natural crystals, such as quartz, exhibit the piezoelectric effect, their electromechanical coupling is too weak to be utilized in engineering fields. In the second half of the last century different types of piezoelectric ceramics were developed, whose electromechanical coupling is sufficiently strong to be employed in actuation devices. Within the piezoceramic family, the typical mixtures of lead (Pb)-zironium (Zr)-titanium (Ti) materials, known as PZT, is widely utilized in robotic fish propulsion system. Piezoelectric materials can produce large stress, but low strain, which limits their application as an actuator [56]. Therefore, special design consideration is required when they are used in propulsion system.

2.3 Smart material-based robotic fish

This section reviews different robotic fish whose actuators are made of smart materials, such as electroactive polymers (mainly IPMC), SMA and piezoelectric material. For IPMC-based and SMA-based robotic fish, only the untethered ones without external power source will be introduced for a fair comparison of swimming speed later. However, the following

piezoelectric robotic fish in this section are all external powered since the piezoelectric robotic fish existing in literature are all tethered.

2.3.1 Electroactive polymers robotic fish

The first conceptual design of an underwater vehicle employing ionic polymers was presented by Shahinpoor in 1991 [57], as shown in Fig. 1. It utilizes an arrangement of electrically controlled ionic polymeric gel muscles. Later, Mojarrad and Shahinpoor built a swimming robotic structure to further investigate this concept, using a polyelectrolyte Ion-Exchange membrane (IEM) as a propulsion fin [18] (Fig. 2). A sheet of Nafion 117 ion exchange membrane, which is chemically treated and plated with platinum, was used as caudal fin actuator. The control and power unit is a small function generator which can produce 4V peak-to peak square wave signal with a frequency up to 50 Hz.

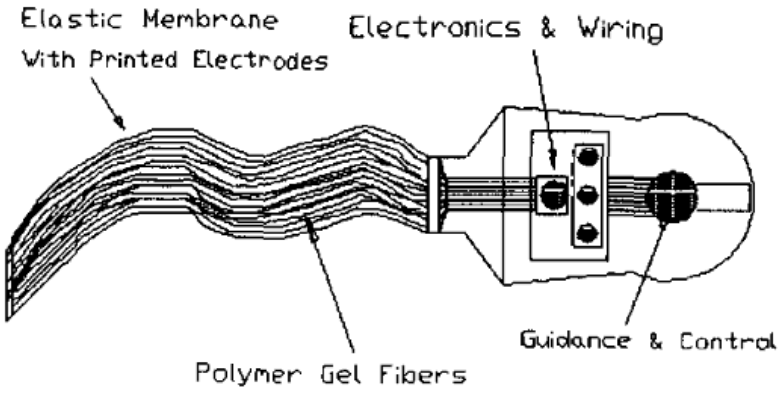

Figure 1. Conceptual design of an IPMC-based Fish [57]. (Reused with permission)

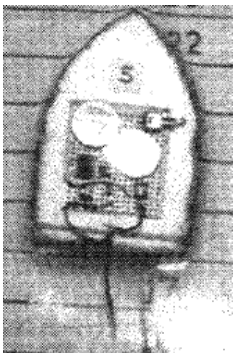

Figure 2. Structure of the experimental swimming robot [18]. (Original source: Proceedings of SPIE--the international society for optical engineering [0277-786X] Mojarrad vol:2716 pg:183) (Reused with permission)

In 2005, Kim *et al* [21] presented a wireless undulatory tadpole robot using IPMC-based actuators. A biomimetic undulatory motion of the fin tail is implemented to improve the thrust of the tadpole robot. The overall body length of the robotic fish is 96 mm, which include the cast IPMC-based actuator, an internal (wireless) power source, and an embedded controller. The motion of the tadpole microrobot can be adjusted by changing the frequency and duty ratio of the input voltage. Swimming speed of 23.6 mm/s is achieved in the undulation motion of the tadpole robot, as shown in Fig. 3 [21].

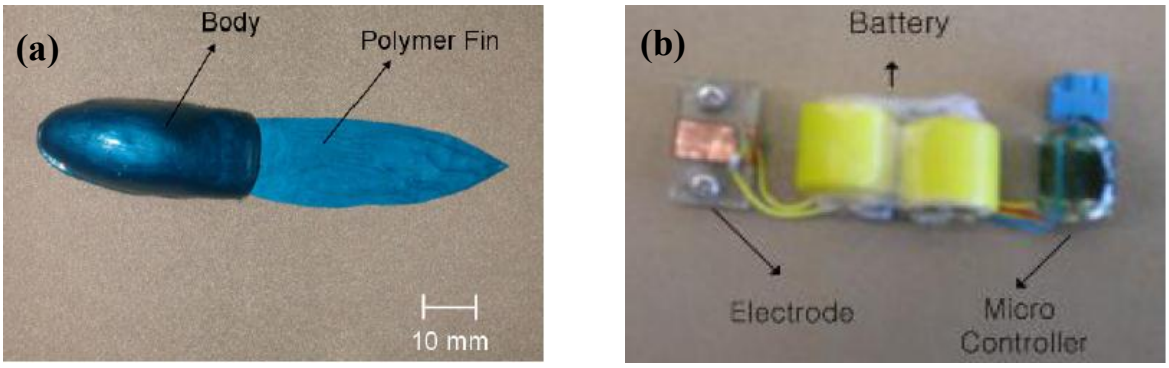

Figure 3. (a) External view of the robot; (b) internal view of the battery, electrode and embedded controller located inside the body [21]. (Reused with permission)

Tan and Kim *et al* [25] developed an IPMC-based robotic fish which integrated GPS receiver, communication system and sensing device. The fish body is directly taken from a toy fish (Swimways Corporation) for housing the electronics. The circuit board is sealed off with silicone adhesive except for the power wires and the interface for reprogramming of the microcontroller. Two rechargeable lithium batteries (3.6 V) are used to generate sufficient power for the electronics and the IPMC. A steady 3.3 V voltage is produced through a voltage regulator for the operation of the circuit and the actuator. The final prototype is 23 × 13 × 6.5 cm and weighs 295 g, as shown in Fig. 4. A peak speed of 6.3 mm/s is achieved at 2 Hz [25].

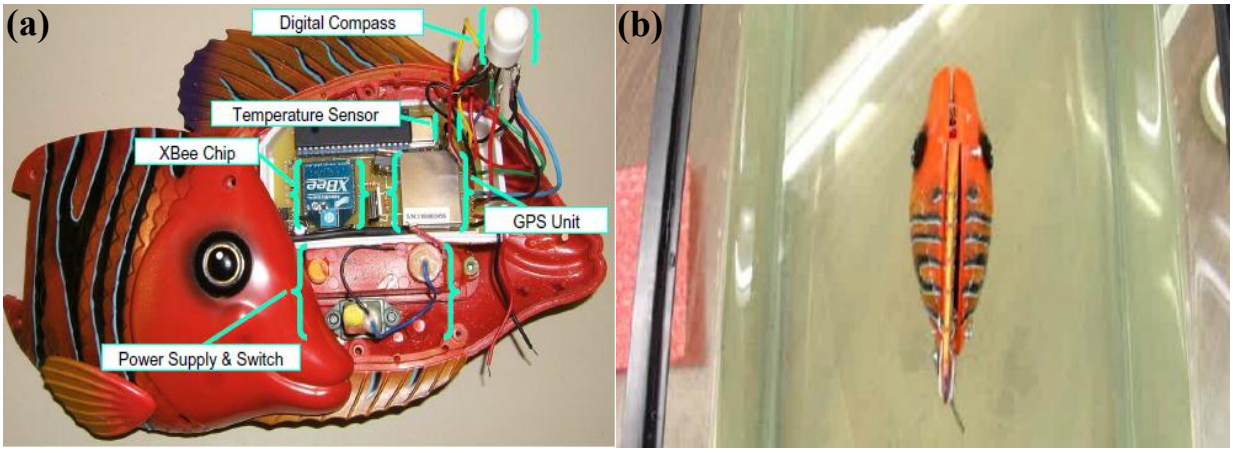

Figure 4. (a) Assembled circuit board for the robotic fish; (b) Robotic fish swimming in the tank [25]. (Reused with permission)

In 2006, Takagi *et al* [58] developed an underwater robot which mimics the swimming form of a ray fish. Its body is made of polystyrene foam. All the electronic components and power system are included in the IPMC-based robotic fish body, such as the microcontroller, the amplifiers, a DC/DC converter, and a lithium ion polymer battery. Sixteen IPMCs are utilized for

fin design. Miniaturization of the electrical devices such as a micro controllers and small amplifiers has been performed for autonomous operation. A simple traveling wave control input is implemented to generate moment on the fin. The total body length of the IPMC-based robotic fish is approximately 90 mm with a speed of 0.8 cm/s, as shown in Fig. 5 [58].

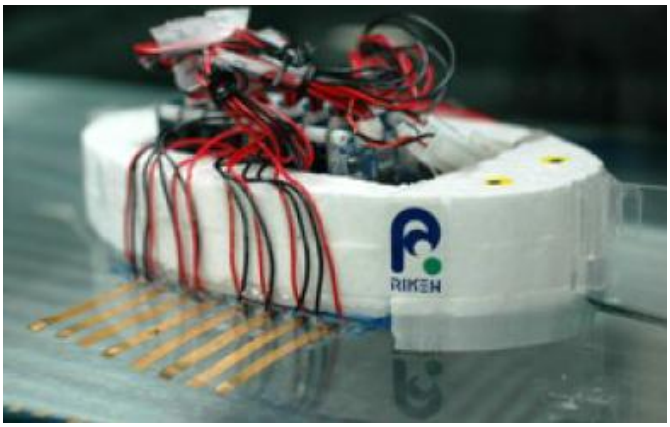

Figure 5. Prototype of the IPMC-based robotic fish [58]. (Reused with permission)

Mbemmo *et al* [26] developed an IPMC-based untethered robotic fish in 2008. The A passive plastic fin covers the IPMC-based actuator to enhance propulsion. All the control unit, sensing unit, power unit and wireless communication unit are inside the robotic fish body. Without the tail, the fish body is 14.8 cm in length. The tail is about 5 cm in length. Therefore, total body length is 19.8cm. The shape and configuration of the robot put the IPMC-based robotic fish into the category of carangiform swimming mode, as shown in Fig. 6. Maximum swimming speed is approximate 2.2cm/s [26].

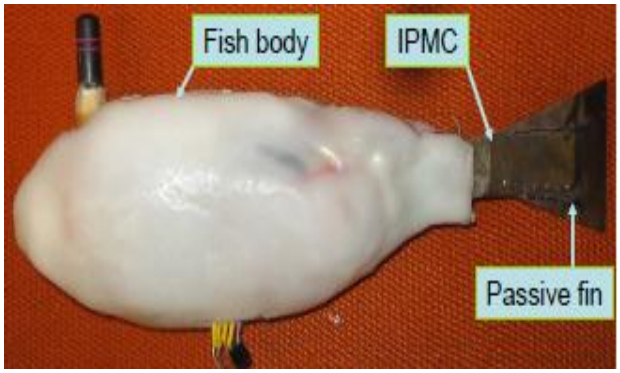

Figure 6. Prototype of the IPMC-based robotic fish [26]. (Reused with permission)

Aureli *et al* [30] developed a modeling frame work for the IPMC-based biomimetic robotic fish, which is validated through experiments on a remotely controlled prototype. This prototype is 13 cm in length, which consists of a small-sized battery pack, an H-Bridge circuit, and a wireless module for remote communication, as shown in Fig. 7. A 2S LiPo battery pack is used as the power source in this robotic fish, which can support approximately 15 min of continuous operation with the overall power consumption being of the order of 1 W. A L2930NE H-Bridge is utilized for controlling the IPMC vibration. The surge speed of this robotic fish is approximately 7.8 mm/s [30].

Figure 7. Prototype of the miniature fish-like robotic swimmer [30]. (Reused with permission)

In 2010, Chen *et al* [29] proposed a physics-based model to predict the steady-state cruising speed of the IPMC-based robotic fish. An IPMC-based robotic fish prototype was developed to test this model. IPMC-based robotic fish was designed to be fully autonomous and serve as a mobile sensing platform, which consists of a rigid body and an IPMC-based caudal fin. A passive plastic fin is used to enhance propulsion. A custom-made rigid shell is employed to reduce the contact surface (or drag force). The total body length of the robotic fish is 22.3cm, with a water drop shape for good hydrodynamic efficiency, as shown in Fig. 8. A swimming speed of 2cm/s is achieved in this prototype [29].

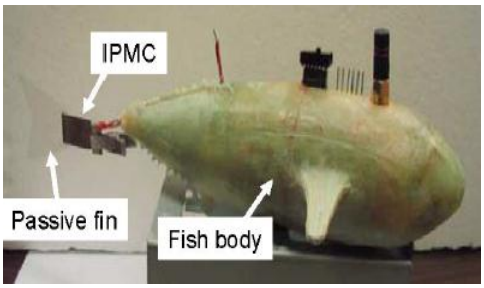

Figure 8. Prototype of the IPMC-based robotic swimmer [29]. (Reused with permission)

Later, Chen *et al* [59] presented a bio-inspired and untethered IPMC-based robotic fish that mimics the cownose ray. The on-board circuit generates a frequency tunable square wave voltage signal to the IPMC actuator in the pectoral fin. The power system consists of a rechargeable 7.3 V Lithium Ion Polymer battery. Two artificial pectoral fins are designed to generate thrust through a twisted flapping motion. For each artificial pectoral fin, IPMC is

utilized as artificial muscle in the leading edge and a passive PDMS membrane is used in the trailing edge. Actuation voltage is applied to the IPMC, and then the passive PDMS membrane follows the bending of IPMC with a phase delay. The total robotic fish is 21cm in length with a speed of 0.7cm/s [59].

In 2011, Chen *et al* [60] presented an underwater robot that mimics the swimming behavior of the manta ray. The artificial pectoral fins are able to generate oscillatory with a large twisting angle. Within each fin, four IPMC actuators are used as artificial muscles. By controlling each individual IPMC strips, the fin can generate complex flapping motions. A lithium ion battery is selected as the power source since it is lightweight and has high power density. In the PCB design, most of the electronic components are in surface-mount package, which makes the circuit board compact (2.5cm by 3cm). Total body length is approximately 8cm. Experimental results show that its swimming speed can be up to 0.055 body length per second (BL/sec) [60].

2.3.2 Shape-memory alloys robotic fish

In 2004, Shinjo and Swain [31] proposed a preliminary design of a biologically inspired Oscillatory Propulsion System using SMA. The use of elastic systems in the scombrid propulsion system was investigated. The activation timing and duration of individual actuators are controlled by a microprocessor. Each actuator is equipped with a simple driver circuit to activate the SMA wires. They adapted a simplified geometry of muscular systems and axial tendons for this design, which alleviate the limited strain of the SMA by trading force for distance and provide an effective force transmission pathway to the backbone [31].

Wang *et al* [61] presented a micro-robot fish propelled by an embedded SMA wire actuated biomimetic fin in 2008. A biomimetic fin (active component) and a caudal fin (passive component) are included in the propulsor. The biomimetic fin can bend to both sides alternatively as the SMA wires of two sides are resistant heated by pulse and cooled in sequence. This SMA robotic fish has no traditional components such as gears and bearings. The control circuit and the power system are inside the body. A radio frequency remote control module and a MCU (PIC16F877A) microcontroller are included in the control circuit. The power system is made by two Li-polymer batteries. This SMA-based robotic fish is 14.6 cm in length with a maximum speed of 112mm/s [61].

Later, Wang *et al* [62] presented a new design of a micro biomimetic manta ray robot fish actuated by SMA wire. The robot fish has a flat-form body and a pair of flexible pectoral fins. The robotic fish body consists of three parts: the dorsal cover, the middle board and the ventral cover. The control module and radio-frequency module is located on the upper surface of the middle board and they are sealed by the dorsal cover. The power system is fixed in the ventral cover, which includes an 11.1 V Lithium polymer rechargeable battery. There is a 111.8 g balance weight embedded in the lower surface of the ventral cover. This prototype is 243mm in length with as maximum speed of 57mm/s [62].

2.3.3 Piezoelectric robotic fish

In 1994, a micro swimming robot driven by PZT was proposed and made [63]. A magnification mechanism was designed to enlarge the displacement of the PZT by 250 times geometrically. Elements in the magnification mechanism are linked with hinges. Each element rotates around a hinge and the displacement of PZT is magnified. Later, they made a prototype of

micro swimming robot in water with a steering mechanism. It can generate forward and backward force by the PZT actuator. The robot is 32 mm in length and 19 mm in width, which does not include power system and control system [2].

Nagata *et al* [64] utilized MFC in their robotic fish prototype in 2008. Several different types of motions were achieved by changing the design of MFC fin. For a single MFC fin, the robotic fish can swim with high speed at resonance frequency. Whirling motion is obtained by adhering two small additional MFCs to generate transverse repulsive force. Locomotion direction can by controlled by adjusting the amplitudes of driving voltages of the MFCs. However, this so-called underwater robot has no internal control unit and power system. External power and control signal are needed to apply to this MFC fin through wire, which limits its free locomotion capability [64].

In 2009, Ming *et al* [5] proposed a mechanism design of MFC-based robotic fish. MSC visual Nastran 4D is used to estimate the resonant frequency in the fluid and analyze the vibration mode. And then they developed a prototype of robot capable of fast motion, forward locomotion and turning motion. A low density material is adhered to the top of the body as a float so that it is easy to balance the entire body and stabilize it near the water surface, as shown in Fig. 9. Single direction propulsive force is obtained through a sine-wave actuation voltage. In order to generate more powerful driving force, two sheets of MFC are pasted on the both side of a carbon plate. However, this prototype still uses external power and control unit through wire connection, which limits its free-locomotion capacity [5].

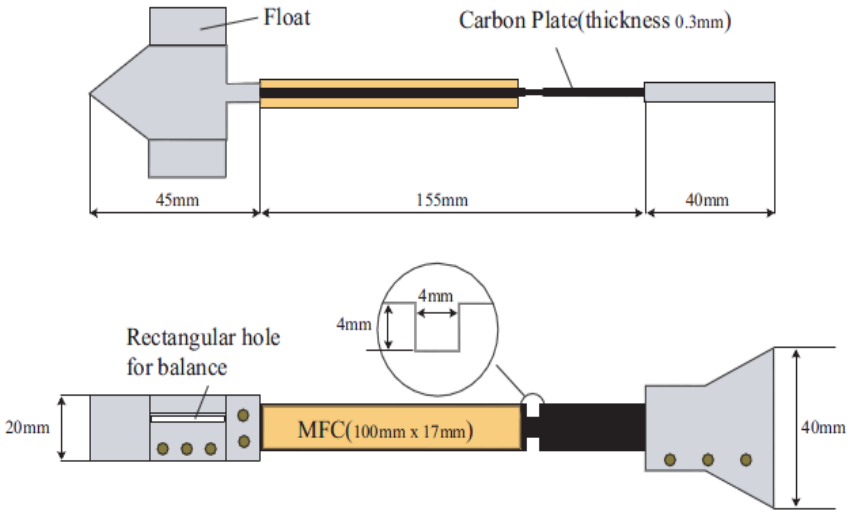

Figure 9. Underwater robot using single carbon-body combined two MFC actuators [5]. (Reused with permission)

Wiguna *et al* [4] presented another prototype of robotic fish using piezoelectric actuators in 2009. PZT is employed in the actuation system, which is composed of two unimorph piezoceramic actuators called lightweight piezo-composite actuators (LIPCAs). In order to generate large vibration amplitude, a linkage system is employed as the magnification mechanism. Two main components of the linkage system are: the rack-pinion system and the four-bar linkage. The rack-pinion system has two racks and one pinion. The rack attached vertically at the center of each LIPCA moves up and down as the LIPCA creates a bending motion, and the pinion attached to the two racks rotates due to the linear motion of the two racks. Because the pinion is assembled together with a long crank, the rotational motion of the pinion causes the long crank to rotate. Similarly, external power source and function generator are necessary to actuate this piezoelectric robotic fish [4].

In 2011, Erturk and Delporte [43] proposed a novel MFC-based robotic fish concept which utilizes both the direct and converse piezoelectric effects. Bimorph MFC fish fins with

and without a passive tail are made and tested under different actuation frequencies. The hydrodynamic thrusts of the robotic fish are measured for the first two harmonic excitation modes, as shown in Fig. 10. They also discussed the feasibility of using converse piezoelectric effect (and solar absorber) to harvest energy at the same time, which leads to the self-powered swimmer-sensor platforms [43].

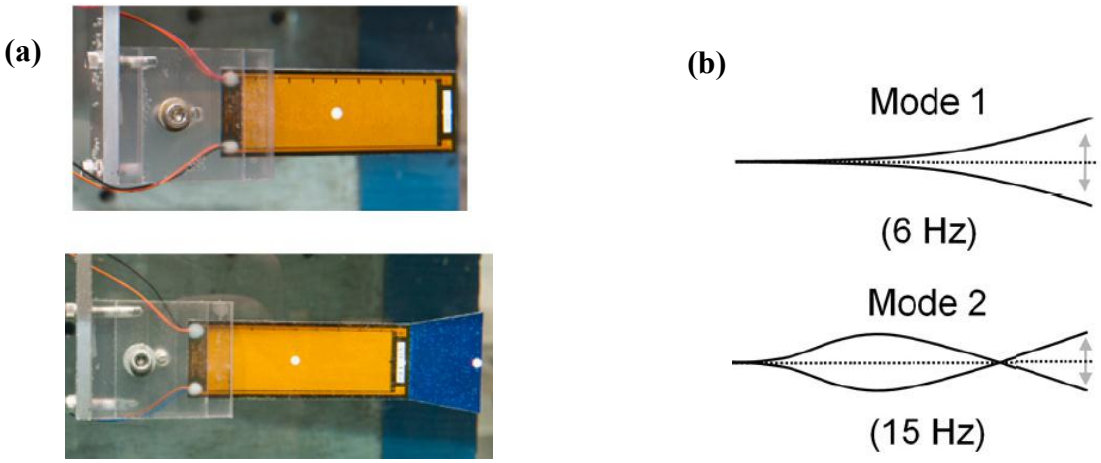

Figure 10. (a) Bimorph fish sample without and with a passive caudal, (b) Mode shapes of the configuration with a passive caudal fin [43]. (Reused with permission)

2.4 Motor-based robotic fish

Besides smart materials, electric motor system is also widely used in robotic fish. In fact, most robotic fish are propelled by motor with mechanical system, such as gear [4]. In order to compare the swimming speed of different robotic fish fairly, in this section, I will also only introduce the untethered motor-based robotic fish with autonomous power system.

In 2000, Hirata [65] studied on a fishlike swimming mechanism and developed a motor-based robotic fish prototype. It has three joints of a tail actuated by two servomotors with an original link mechanism, which can simulate various moving patterns optionally. The servomotors, an R/C receiver and a battery are set in a body that is waterproof by rubber rings

and linear bearings. Swimming speed of the prototype fish robot is measured at a water tank which has 8 m length, 0.9 m width and 1.2 m depth. After the pre-swimming of about 4 m to have a stable velocity, the measurement to get the swimming speed begins. The maximum swimming speed is 40 cm/s with about 60 cm body length [65].

Later Hirata *et al* [66] developed a motor-based robotic fish with good dynamics performance. Turning modes for the fish robot that uses tail swing are discussed. The tail fin of the prototype fish robot is made of hard wood in order to keep a setting motion strictly. The prototype fish robot has only two joints at a tail peduncle and a tail fin. They utilized two servomotors for a radio control model (R/C) to drive each joint. The servomotors are controlled by a personal computer with a R/C transmitter and a D/A converter. A control program on the personal computer realizes various motion patterns. The maximum swimming speed is about 0.2 m/s in the experiment. The body length of this motor-based robotic fish prototype is 34 cm [66].

In 2005, Fan *et al* [67] developed a free-swimming, radio-controlled, multi-link biomimetic robotic dolphin mimicking dorsoventral movement. The thrust is produced by the up-down-motioned fluke, and the turning is achieved by its left-right-sided body deflecting. Four servomotors are connected in series within the control unit to mimic dorsoventral movement, which are controlled by PWM signals. These servomotors act on a dolphin-shaped, flexible backbone. As for the propulsion unit, the link-based tail generates the main propulsive force. The first servomotor is fixed vertically to produce the force to bend the tail when turning. The other three are installed horizontally that oscillate in vertical plane to generate thrust. The speed of the robotic dolphin's straight motion is controlled by modulating the links' oscillating frequency amplitude. It is 55cm in length, which has a maximum speed of 22 cm/s [67].

Hu *et al* [68] built nine generations of robotic fish in their robotic fish research project at Essex in 2006. This motor-based robotic fish utilizes 3 powerful R/C servo motors and 2 DC motors. Three servo motors are concatenated together in the tail to act as 3 joints. One DC motor is used to change the center of gravity of the fish, which is fixed in the head. And another DC motor controls the micro-pump. A dorsal fin is fixed vertically on the back of the fish body to keep fish from swaging. The head of the robotic fish is waterproofed and all of electronic components and motors are protected. Its body length is about 52 cm with a maximum swimming speed of 50 cm/s [68].

In 2007, Shin *et al* [69] developed a motor-based robotic fish to imitate the ways real fish swim. Four servo motors are implemented at the caudal fin of the robot for propulsion and horizontal direction control. Three IR distance sensors and four sonar sensors are utilized for obstacle detection, which are mounted at the front and two sides of the head. The power system consists of two battery packs. Each of these packs has two parallel-connected 1.2V*4 Ni-MH battery set. One battery pack solely supplies power to the motor. Another one supports power for microcontroller, sensor, etc. This motor-based robotic fish has a total body length of 78 cm and a maximum swimming speed of 72 cm/s [69].

Later, Papadopoulos *et al* [70] made a motor-based robotic fish, which includes the tail's motion control system, the wireless communication system, and the autonomous power system. This power system can support the swimming of robotic fish for at least one hour. It consists of a battery pack of five AAA NiMH cells, each having 550 mAh capacity. In addition, two Maxim MAX603C 500 mA linear voltage regulators provide 5 V fixed supply to the motor driver IC and to the rest of the ICs separately so as to isolate the electric noise produced by the motor driver.

An assembly of pulleys and cables was utilized to transmit the motion to the tail. The total body length is 33.7 cm. It has a maximum swimming speed of 17.2 cm/s [70].

In 2009, Wang *et al* [71] made an amphibious robot inspired by various amphibian principles in animal kingdom. They proposed a hybrid propulsive mechanism that integrates fish-like swimming with wheel paddle- fin movements. Both servo motor and DC motor are utilized in this motor-based robotic fish. The servo drives the inner shaft via a gear set with a reduction ratio of 1:2, which allows the flipper to forward flapping or reversing flapping in a range of from 0 to 360 degree. The DC motor (Maxon RE 16, with a locked torque of 28.8mN) can provide larger torque, which can drive the outer shaft through a bevel gear set corresponding to a revolution direction change of 90 degree. The head and each fishlike propelling module carry Li-Polymer batteries for actuators. Maximum swimming speed of 45 cm/s is obtained with a total body length of 70 cm [71].

A motor-based robotic fish was developed in Nanyang Technological University in 2011 [72], which consists of four individual modules: tail fin module, electronics housing module, ballast tank module and head module (including sensors and power unit). A caudal fin is used to provide the propulsion, which is driven by a DC motor and a set of miter gears to convert the horizontal axis of rotation into vertical axis. The last joint of the tail fin has a spring-loaded passive joint, which can provide some degree of flexibility to the tail fin mechanism. The microprocessor, motor controllers, radio frequency receiver and navigation sensor for the robotic fish are located in the electronics housing module. This motor-based robotic fish is 66.1 cm in length, which has a maximum swimming speed of 33 cm/s [72].

2.5 Comparison between smart material-based and motor-based robotic fish

Smart material- based robotic fish is relatively new, which is still in its early stage of development. Generally speaking, current motor-based robotic fish have a larger speed per body length compared to current smart material-based ones. However, this motor and gear system inside the robotic fish will generate large noise. In addition, the motor-based robotic fish tends to have a much larger size compared to the smart material -based ones since the complexity of the motor-gear system. A comparison table between different untethered robotic fish is shown in Fig. 11 and table 1.

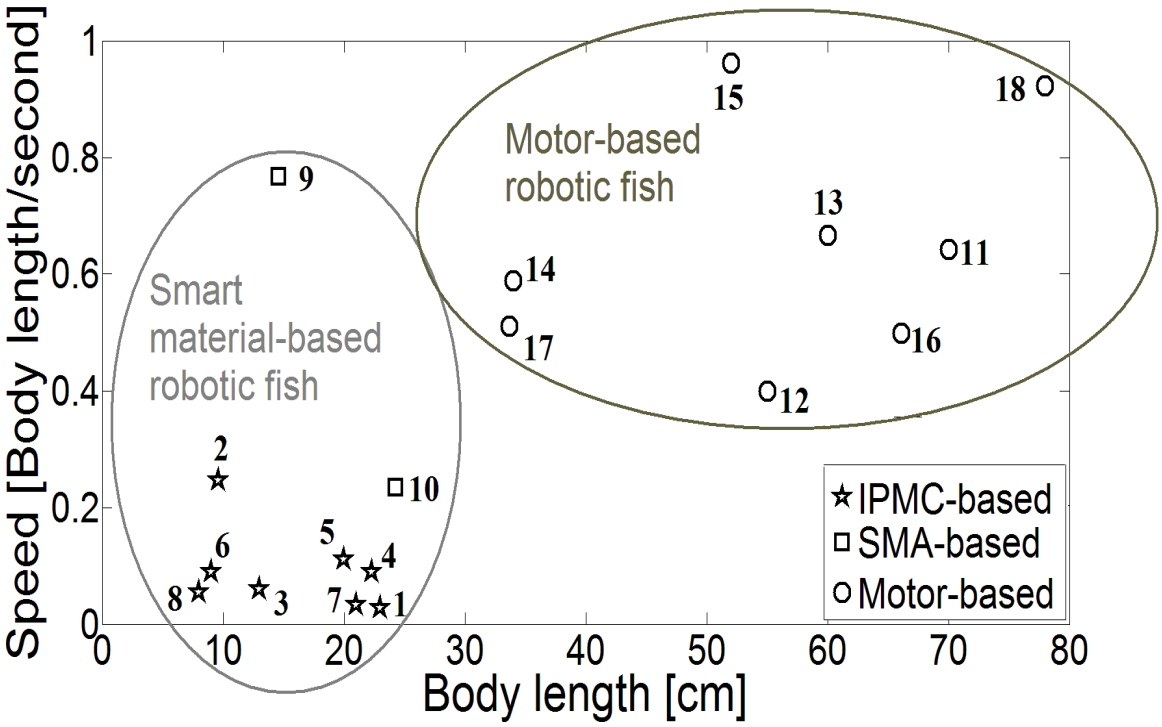

Figure 11. Comparison of smart material-based and motor-based untethered robotic fish. (speed per body length vs. robot length)

Table 1. Table for smart material-based and motor-based untethered robotic fish.

Reference	Label in Fig. 11	Sources
IPMC		
[25]	**1**	X. Tan *et al* (2006)
[21]	**2**	B. Kim *et al* (2005)
[30]	**3**	M. Aureli *et al* (2010)
[29]	**4**	Z. Chen *et al* (2010)
[26]	**5**	E. Mbemmo *et al* (2008)
[58]	**6**	K. Takagi *et al* (2006)
[73]	**7**	Z. Chen *et al* (2011 November)
[60]	**8**	Z. Chen *et al* (2011 April)
SMA		
[61]	**9**	Z. Wang et al (2008)
[62]	**10**	Z. Wang et al (2009)
Motor		
[71, 74]	**11**	R. Ding et al (2009)
[67]	**12**	R. Fan et al (2005)
[75]	**13**	K. Hirata (2000)
[76]	**14**	K. Hirata et al (2000)
[77, 78]	**15**	H. Hu (2006)
[79, 80]	**16**	K. H. Low (2011)
[70]	**17**	E. Papadopoulos et al (2009)
[81, 82]	**18**	D. Shin et al (2007)

Among all smart materials, the IPMC technology [17-30] has received great interest for biomimetic locomotion primarily due to its low-voltage actuation and large-amplitude deflection capabilities.

Similar to IPMCs, MFC piezoelectric actuators also exhibit high efficiency in size, reduced energy consumption, and noiseless performance. In addition, MFCs offer large dynamic stresses in bending actuation as well as high performance for both low-frequency and high-frequency applications. Piezoelectric materials offer strong electromechanical coupling, large power density, and their fabrication methods at different scales are well established [83-86]. From the point of view of multifunctionality, the converse piezoelectric effect can be used for

dynamic actuation in biomimetic locomotion at low-to-moderate frequencies, while the direct piezoelectric effect can be employed for harvesting underwater energy toward enabling self-powered swimmer-sensor platforms [43].

To the best of our knowledge, untethered piezoelectric robotic fish (without external power supply) does not exist in the literature [2-5]. High voltage input requirement and low strain output are the two downsides of piezoelectric transduction limiting the application of previously investigated piezoelectric structures for robotic fish development to use in free locomotion. In order to overcome the shortage of low strain in piezoelectric robotic configurations prior to the MFC technology, various magnification mechanisms were proposed by others [2-4]. However, the magnification component that is employed for creating larger vibration amplitudes might create noise and cause additional energy loss. As far as the high input voltage requirement is concerned, research groups used tether connection to external power source, which restricts the free-locomotion capability [2-5].

2.6 Significance of the current research

In this thesis, an untethered piezoelectric (MFC-based) robotic fish prototype is developed and tested in free locomotion. High voltage input requirement and low strain output limit the application of piezoelectric material in untethered robotic fish. To the best of our knowledge, no untethered piezoelectric robotic fish exist before in the literature [2-5]. In order to reduce noise and power consumption, no traditional magnification components are employed, such as gears and bearings. An MFC-based bimorph fin and an autonomous power system are employed to overcome the shortages of piezoelectric material (low strain and high input voltage).

The untethered prototype serves to show the promising prospect of piezoelectric fish-like propulsion.

A swimming speed of a 0.3 body length per second (7.5 cm/s swimming speed for 24.3 cm body length) is achieved. This swimming speed of the first prototype can be improved substantially by increasing the actuation voltage, optimizing the volume, and using a caudal fin extension. The preliminary MFC-based untethered robotic fish shows its advantage in swimming speed compared to current untethered IPMC-based robotic fish. Comparing to motor-based, it has advantage in size reduction, low-noise and energy efficiency.

At the meantime, the MFC piezoelectric bimorph fin is investigated theoretically and experimentally. First the in-air and underwater dynamics of an MFC bimorph cantilever is modeled for linear bending vibrations under dynamic piezoelectric actuation. The in-air electroelastic model is extended to obtain an underwater electrohydroelastic model accounting for the hydrodynamic effects following the work by Sader and others [6-9]. In-air and underwater experiments are conducted for model validation and for characterizing a bimorph propulsor.

In addition, a thrust estimation model that couples the actuator dynamics and hydrodynamic effect is essential to optimal design and control of biomimetic robotic fish. Even though there is no complete theory for estimating the thrust of vibrating cantilever beams in placid environment [13], many IPMC-based robotic fish groups still tried many different theories in thrust estimation for IPMC beam. Similarly, a thrust estimation model for piezoelectric cantilever beam will also be essential in the future optimization of the piezoelectric robotic fish design.

In this thesis, Lighthill's slender-body theory [10-12] is used to predict the thrust output in quiescent water by reducing Lighthill's mean thrust expression to the quiescent water condition. This classical Lighthill's slender body theory has been used in IPMC-based robotic fish group to predict the steady-state cruising speed [26, 29]. They equalized the thrust expressions from reactive and resistive method to derive the cruising speed. The drag coefficient needs to be identified in advance by metric spring scales when pulling the fish with different velocities. In this thesis, only the reactive method (Lighthill's slender body theory) is employed to estimate the thrust in quiescent water condition. No drag coefficient identification is needed in this case.

CHAPTER 3

THEORY

3.1 Piezohydroelastic modeling of in-air and underwater dynamic actuation

3.1.1 In-air dynamics of a bimorph propulsor

The linear electroelastic equation of motion for in-air vibrations of a thin bimorph cantilever (Fig. 12) under dynamic voltage actuation is given by

$$D\frac{\partial^4 w(x,t)}{\partial x^4}+m\frac{\partial^2 w(x,t)}{\partial t^2}+c\frac{\partial w(x,t)}{\partial t}=\vartheta\left[\frac{d\delta(x)}{dx}-\frac{d\delta(x-L)}{dx}\right]v(t) \tag{1}$$

where D is the flexural rigidity of the composite cross section, m is the mass per length, c is the damping coefficient, ϑ is the space-independent electromechanical coupling term in the physical coordinates, $\delta(x)$ is the Dirac delta function, $v(t)$ is the actuation voltage, and $w(x,t)$ is the deflection of the reference surface in the transverse (z) direction at the longitudinal position x and time t. Here, m and c are altered in underwater vibrations due to the added mass and damping effect of hydrodynamic loads as discussed in Section 3.1.2.

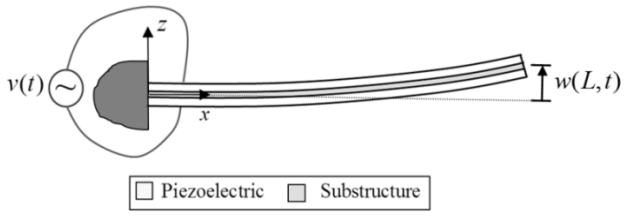

Figure 12. Schematic of a uniform cantilevered bimorph propulsor under dynamic voltage actuation to create bending vibrations (piezoelectric layers can be combined in series or in parallel).

Separating the spatial and temporal variables with the single-mode (fundamental mode) assumption yields

$$w(x,t) \cong \phi(x)\eta(t) \tag{2}$$

where $\phi(x)$ and $\eta(t)$ are the mass-normalized eigenfunction and the modal coordinate of the fundamental transverse vibration mode for a clamped-free uniform beam. The mass-normalized eigenfunction for the first mode can be obtained as

$$\phi(x) = \sqrt{\frac{1}{mL}}\left[\cosh\frac{\lambda x}{L} - \cos\frac{\lambda x}{L} - \sigma\left(\sinh\frac{\lambda x}{L} - \sin\frac{\lambda x}{L}\right)\right] \tag{3}$$

and it satisfies

$$\int_0^L m\phi^2(x)dx = 1, \quad \int_0^L \phi(x)D\frac{d^4\phi(x)}{dx^4}dx = \omega_{n,air}^2 \tag{4}$$

Here, $\lambda = 1.87510407$, $\sigma = 0.734095514$, L is the length of the bimorph, and $\omega_{n,air}$ is the in-air natural frequency:

$$\omega_{n,air} = \lambda^2\sqrt{\frac{D}{m_s L^4}} \tag{5}$$

where m_s is the structural mass per length.

For in-air vibrations, the mass per length in Eq. (1) is merely the structural mass per length:

$$m = m_s \tag{6}$$

while the in-air damping coefficient is

$$c = 2m_s\zeta_s\omega_{n,air} \tag{7}$$

where ζ_s is the in-air damping ratio which is assumed to be dominated by structural and other mechanical losses for in-air vibrations.

Following the standard analytical modal analysis procedure [87], i.e., substituting Eq. (2) into Eq. (1), multiplying the latter by the eigenfunction and integrating the resulting equation over the beam length, one obtains

$$\frac{d^2\eta(t)}{dt^2}\int_0^L m\phi^2(x)dx+\frac{d\eta(t)}{dt}\int_0^L c\phi^2(x)dx+\eta(t)\int_0^L \phi(x)D\frac{d^4\phi(x)}{dx^4}dx=v(t)\int_0^L \phi(x)\vartheta\left[\frac{d\delta(x)}{dx}-\frac{d\delta(x-L)}{dx}\right]dx \tag{8}$$

yielding

$$\frac{d^2\eta(t)}{dt^2}+2\zeta_s\omega_{n,air}\frac{d\eta(t)}{dt}+\omega_{n,air}^2\eta(t)=\theta v(t) \tag{9}$$

where θ is the electromechanical coupling term in the modal coordinates:

$$\theta=\int_0^L \phi(x)\vartheta\left[\frac{d\delta(x)}{dx}-\frac{d\delta(x-L)}{dx}\right]dx=\vartheta\frac{d\phi(x)}{dx}\bigg|_{x=L} \tag{10}$$

If the actuation voltage is assumed to be harmonic of the form

$$v(t)=V_0e^{j\omega t} \tag{11}$$

where V_0 is the actuation voltage amplitude, ω is the actuation frequency (in rad/s), and *j* is the unit imaginary number, then the steady-state response for the modal coordinate is

$$\eta(t)=\frac{\theta V_0e^{j\omega t}}{\omega_{n,air}^2-\omega^2+j2\zeta_s\omega_{n,air}\omega} \tag{12}$$

The resulting in-air tip velocity amplitude is therefore

$$\left|\frac{\partial w(L,t)}{\partial t}\right|\cong\left|\phi(L)\frac{d\eta(t)}{dt}\right|=\left|\frac{V_0\omega\theta\phi(L)}{\omega_{n,air}^2-\omega^2+j2\zeta_s\omega_{n,air}\omega}\right| \tag{13}$$

from which the tip velocity – to – actuation voltage frequency response function (FRF) can be extracted.

It is important to note that this solution is valid for excitations around the fundamental natural frequency since higher vibration modes are not used in Eq. (2). In addition, the foregoing

derivation neglects the geometric, material, and dissipative nonlinearities [88-90] and is strictly valid for linear vibrations only.

3.1.2 Underwater dynamics of a bimorph propulsor

In this section, hydrodynamic effects are included to predict the underwater vibrations of the cantilever following the previous work by Sader and others [6-8]. Similar efforts are due to Mbemmo et al. [26] and Aureli et al. [30] for the underwater dynamics of IPMC propulsors. The assumptions on the structure and fluid in this approach can be stated as follows [6-8]: (1) the beam is uniform along its length; (2) length of the beam is much larger than the other two dimensions; (3) the vibration amplitude is much smaller than the length and width in the beam; and (4) the surrounding fluid is unbounded in space.

According to assumption (2), Sader's hydrodynamic theory will be better satisfied when the aspect ratio (ratio between length and width) of the actuator is larger. However, in practice, robotic fish's aspect ratio for actuator is just around 2 to 3 when applying Sader's hydrodynamic function [26, 29]. In our case, the aspect ratio is just 2.6 for this specific MFC bimorph. This may be a reason for the discrepancy between the estimated and measured values shown in Fig. 20.

The added mass per length m_a and the hydrodynamic damping ratio ζ_h can be expressed in terms of the hydrodynamic function Γ as [6, 91]

$$m_a = \frac{\pi \rho_w b^2}{4} \Gamma_r \tag{14}$$

$$\zeta_h = \frac{1}{2Q_h} = \frac{\Gamma_i}{2\left(\frac{4m_s}{\pi \rho_w b^2} + \Gamma_r \right)} \tag{15}$$

where ρ_w is the mass density of water, Q_h is the quality factor due to hydrodynamic damping, Γ_r and Γ_i are the real and imaginary parts of hydrodynamic function Γ, respectively, and b is the width of the bimorph propulsor.

The hydrodynamic function Γ can be calculated analytically or numerically. In this thesis, we use the $\Gamma(\mathrm{Re})$ expression following Sader's work [6], which is a function of the Reynolds number (Re):

$$\Gamma(\mathrm{Re}) = \Omega(\mathrm{Re})\left[1 + \frac{4jK_1\left(-j\sqrt{j\,\mathrm{Re}}\right)}{\sqrt{j\,\mathrm{Re}}K_0\left(-j\sqrt{j\,\mathrm{Re}}\right)}\right] \tag{16}$$

where the Reynolds number depends on the frequency through

$$\mathrm{Re} = \frac{\rho_w \omega b^2}{4\mu} \tag{17}$$

Here, $\Omega(\mathrm{Re})$ is the correction function to approximate the Γ of rectangular beam from circular cylinder, K_0 and K_1 are the modified Bessel functions of the third kind, μ is the viscosity of water, and the length scale is the width b [6].

$$\Omega(\mathrm{Re}) = \Omega_r(\mathrm{Re}) + i\Omega_i(\mathrm{Re}) \tag{18}$$

$$\tau = \log_{10}\mathrm{Re} \tag{19}$$

$$\begin{aligned}\Omega_r(\mathrm{Re}) = {} & (0.91324 - 0.48274\tau + 0.46842\tau^2 - 0.12886\tau^3 \\ & + 0.044055\tau^4 - 0.0035117\tau^5 + 0.00069085\tau^6) \times (1 - 0.56964\tau \\ & + 0.4869\tau^2 - 0.13444\tau^3 + 0.045155\tau^4 - 0.0035862\tau^5 + 0.00069085\tau^6)^{-1},\end{aligned} \tag{20a}$$

$$\begin{aligned}\Omega_i(\mathrm{Re}) = {} & (-0.024134 - 0.029256\tau + 0.016294\tau^2 - 0.00010961\tau^3 \\ & + 0.000064577\tau^4 - 0.00004451\tau^5) \times (1 - 0.59702\tau + 0.55182\tau^2 \\ & - 0.18357\tau^3 + 0.079156\tau^4 - 0.014369\tau^5 + 0.0028361\tau^6)^{-1},\end{aligned} \tag{20b}$$

$\Omega(\mathrm{Re})$ is expressed as a rational function in $\log_{10}\mathrm{Re}$, whose unknown coefficients are then evaluated by performing a nonlinear least-squares fit with the numerical data over the range $\mathrm{Re}\in[10^{-6},10^{4}]$. It is accurate to within 0.1% over the entire range $\mathrm{Re}\in[10^{-6},10^{4}]$ for both real and imaginary parts [6]. Some other simplified expressions of the hydrodynamic function Γ are also available depending on the range of Re [92, 93]. In this thesis, we will only use Eq. (16), which has a good accuracy for a wide range of Re.

According to assumption (3), Sader's hydrodynamic function Γ only works well when the vibration amplitude is small (linear case). In the case of large amplitude vibration, a correction term $\Delta\Gamma(\mathrm{Re},\kappa)$ should be added to Sader's hydrodynamic function Γ to take into account the added mass and damping due to vortex shedding, as shown below [93, 94]:

$$\Theta(\mathrm{Re}) = \Gamma(\mathrm{Re}) + \Delta\Gamma(\mathrm{Re},\kappa) \tag{21}$$

where $\Theta(\mathrm{Re})$ is the hydrodynamic function for large amplitude vibration, κ is the Keulegan-Carpenter number, which represents the ratio of the vibration amplitude to the body diameter. For small vibration ($\kappa \approx 0$), $\Delta\Gamma(\mathrm{Re},0)\approx 0$. In this thesis, $\Delta\Gamma(\mathrm{Re},\kappa)$ is only identified from experiment. Nonlinear modeling for hydrodynamic function $\Theta(\mathrm{Re})$ will be future work.

The Reynolds number quantifies the relative importance of inertial and viscous effects [91]. Viscous effects play a dominant role for microscopic beams (e.g., ~100 μm in length, $\mathrm{Re}\sim O(1)$) and become negligible for macroscopic beams (~1m in length) [6, 7, 9]. For the bimorph propulsor discussed in this work (L = 90.2 mm, b = 35 mm), both structural and hydrodynamic dampings are taken into account for the total damping ratio ζ_w of underwater vibration [29]:

$$\zeta_w = \zeta_s + \zeta_h \tag{22}$$

For underwater vibrations, the mass per length and damping coefficient terms in Eq. (1) are

$$m = m_w = m_s + m_a \tag{23}$$

$$c = 2m\zeta_w\omega_{n,water} = 2m_w(\zeta_s + \zeta_h)\omega_{n,water} \tag{24}$$

and the mass-normalized eigenfunction in Eq. (2) satisfies

$$\int_0^L m\phi^2(x)dx = 1, \quad \int_0^L \phi(x)D\frac{d^4\phi(x)}{dx^4}dx = \omega_{n,water}^2 \tag{25}$$

The underwater natural frequency $\omega_{n,water}$ is obtained from the in-air natural frequency $\omega_{n,air}$ (which is approximately the in-air resonance frequency for $\zeta_s \ll 1$) through Chu's formula modified by the real part of the hydrodynamic function Γ_r [6]:

$$\omega_{n,water} = \omega_{n,air}\sqrt{1 + \frac{\pi\rho_w b^2}{4m_s}\Gamma_r} \tag{26}$$

where $\omega_{n,air}$ is given by Eq. (5). Again, Eq. (26) only works well for linear case (small amplitude vibration).

The resulting underwater tip velocity response amplitude is therefore

$$\left|\frac{\partial w(L,t)}{\partial t}\right| \cong \left|\phi(L)\frac{d\eta(t)}{dt}\right| = \left|\frac{V_0\omega\theta\phi(L)}{\omega_{n,water}^2 - \omega^2 + j2\zeta_w\omega_{n,water}\omega}\right| \tag{27}$$

where θ is due to Eq. (10). However, the eigenfuction $\phi(x)$ in Eq. (10) is normalized according to Eq. (25) with *m* given by Eq. (23).

3.2 Thrust estimation method

Thrust generation has been commonly related to two possible parts of fish: (1) the sides of the body pushing obliquely backward (as in a swimming eel), or (2) the tail fin (as in fast

swimmers such as the tuna) [49]. However, direct visualization of thrust generation is a complicated task [95], and controversies exist regarding the theories of fish locomotion [46]. As suggested by Peterson *et al* [13], no complete theory is currently available for estimating the thrust production of vibrating cantilever beams in placid environment.

A thrust estimation model that couples the actuator dynamics and hydrodynamic effect is essential to optimal design and control of biomimetic robotic fish. Two main classical methods have been widely used in thrust calculation for robotic fish [21, 29, 30, 38, 39, 49]. One of these methods is Taylor's *resistive* model theory. In this method, thrust is estimated by the total drag force, which requires the identification of the drag coefficient for the fish body [96, 97]. The other method is the *reactive* method, which is based on Lighthill's elongated-body theory [10-12]. The reactive method, or the elongated-body theory, is based on the reactive forces between the "virtual mass" of water and the body. During swimming, the fish body exerts a force to the surrounding water. Consequently, the water will generate an equal reaction force on the fish body. Therefore, the thrust can be estimated through this reaction force.

3.2.1 Resistive method

In this resistive method, the force between a small section of the animal and the water was considered as a resistive force depending exclusively on the instantaneous value of the velocity of that section relative to the water [98].

Taylor began to analysis the motion of microscopic organisms in 1951, and started to consider the swimming of larger animals such as snakes and worms in 1952. Eel-like animals was treated as chains of short segments. He multiplied the resistive force by the velocity of the

segment to obtain the power required to move it and integrated over the length of the body to obtain the total power requirement for swimming [96, 99-101].

Examples using resistive method can be found in IPMC-based robotic fish papers [26, 29]. At the steady state, mean thrust (*T*) is balanced by the drag force F_D, which is shown as below:

$$F_D = \frac{1}{2} C_D \rho_w U^2 S \tag{28}$$

where C_D is the drag coefficient, *U* is the swimming speed, *S* is the wetted surface area.

The drag coefficient C_D need to be identified experimentally before estimating the thrust using Eq. 28. In order to identify C_D, they pulled the fish with different velocities, and the corresponding drag forces F_D were measured by metric spring scales. Fig. 13 illustrates the experimental setup for drag force measurement [26, 29].

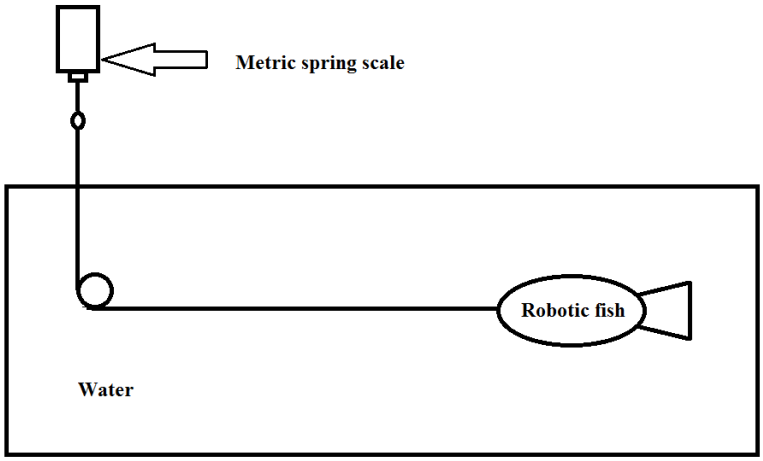

Figure 13. Experimental setup for the drag force measurement.

With the measured drag force, velocity, and surface area of the fish, the drag coefficient C_D can be calculated from Eq. 28. Through drag force measurement, one can get the plot of the drag force versus velocity. Based on Eq. 28, one can fit the experimental data with simulation data through the least-squares method to identify the drag coefficient.

3.2.2 Reactive method

The reactive method emphasizes on reactive forces between a small volume of water and the parts of the animal's surface in contact with it. These forces, due to the inertia of the water and proportional to rate of change of the relative velocity of animal surface which a given volume of water feels, are neglected on the resistive theory. They can be particularly important when the cross-section of the animal is much thinner in the direction of the bodily displacements that it makes for swimming purposes than in a perpendicular direction; then, the "virtual mass" of water which acquires momentum through such displacements far exceeds the associated animal mass. A famous reactive method is the elongated body theory [48, 98, 102].

In 1951, Sir G. I. Taylor discussed the problem of swimming microscopic organisms in viscous fluid [96, 99]. Later on he investigated the swimming of long narrow animals [100]. Based on the "slender body theory" from aerodynamics, Lighthill (1960) proposed the elongated-body (slender body) theory and then extended it to take into account fish motions of arbitrary amplitude, leading to the large-amplitude elongated-body theory in 1971 [98, 102]. The elongated body theory has been widely used to describe the anguilliform, subcarangiform, and carangiform locomotion modes.

During swimming, the propulsive element exerts a force to the water passing backward. Consequently, an equal reaction force F_R is generated by the water on the body. Neglecting

viscous effects since the Reynolds numbers of adult fish is between $10^3 < Re < 10^6$ [49], the magnitude of F_R can be approximated as the product of the water mass accelerated and its acceleration. F_R can be divided into lateral component F_L and thrust component F_T (Fig. 24). The propulsion is primarily related to the thrust F_T component, while the lateral component F_L , which sheds water laterally, can cause energy losses [49, 101]. Therefore, based on the principle of energy conversion, the thrust power is the difference between the total power and the wake power. A fundamental assumption in Lighthill's theory is that the cross-sectional area of the body changes slowly along its length [26, 29].

The mean thrust (T) in Lighthill's theory [10-12] is given in the presence of an external relative free stream of speed U (which is essentially the swimming speed) as

(Detail derivation is in Appendix A)

$$T = \frac{1}{2} m_v \left[\overline{\left(\frac{\partial w}{\partial t} \right)^2} - U^2 \overline{\left(\frac{\partial w}{\partial x} \right)^2} \right]_{x=L} \tag{29}$$

where the over-bar stands for the mean value, m_v is the virtual mass per length at $x = L$, expressed as

$$m_v = \frac{\pi \rho_w b^2}{4} \alpha \tag{30}$$

where α is a virtual mass coefficient close to 1 [26, 29].

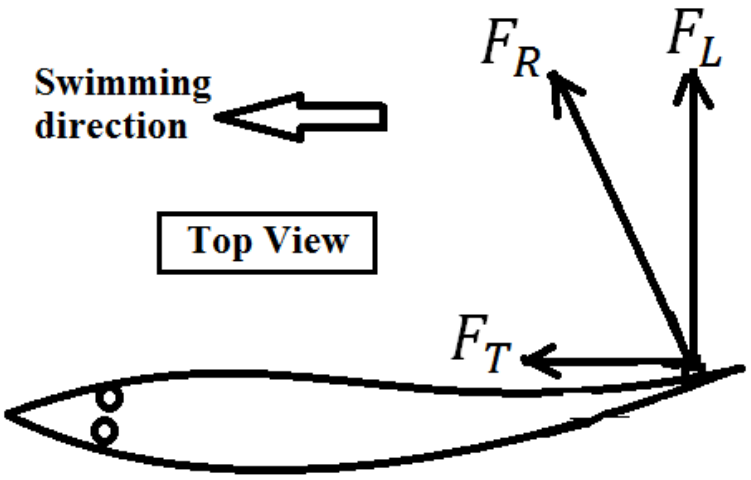

Figure 14. Thrust generation by the reactive method.[49]

In most cases of robotic fish thrust estimation [29, 30, 37-39], it becomes necessary to identify certain calibration factors, such as the drag coefficient, which removes the possibility of obtaining an *a priori* estimate of the thrust resultant solely from the underwater vibration response. In this research, Lighthill's slender-body theory [10-12] is utilized to estimate the mean thrust in quiescent water as a first approximation.

Here, we set $U \to 0$ to approximate quiescent water condition and reduce Eq. 29 to

$$T \cong \frac{1}{2} m_v \overline{\left(\frac{\partial w}{\partial t} \right)^2 \Bigg|_{x=L}} = \frac{\pi \rho_w b^2}{8} \overline{\left(\frac{\partial w(L,t)}{\partial t} \right)^2} \tag{31}$$

where the mean thrust T depends only on the tail tip velocity and the virtual mass for quiescent water condition.

This classical Lighthill's slender body theory has been used in IPMC-based robotic fish group to predict the steady-state cruising speed [26, 29]. They equalized the trust expressions from reactive and resistive method to derive the cruising speed. The drag coefficient was measured by metric spring scales when pulling the fish with different velocities.

In this thesis, only the reactive method (Lighthill's slender body theory) is used to estimate the thrust in quiescent water condition. No drag coefficient identification is needed in this case. In the future work, additional device will be built to identify the drag coefficient for cruising speed estimation.

CHAPTER 4

EXPERIMENTAL METHODS

4.1 Setup for in-air tip velocity FRF measurements

The MFC bimorph tested and characterized in the experiments is shown in Fig. 15 and Fig. 16 along with its clamp and fixture employed for the in-air actuation FRF measurements. The basic geometric and structural properties of the bimorph are given in Table 2. The electrode leads of the two MFCs are combined in parallel throughout the experiments discussed in this thesis. A vertically aligned laser vibrometer is used along with the monitored actuation signal in order to obtain the transverse (vertical direction in Fig. 15) tip velocity – to – actuation voltage FRFs of the MFC bimorph in air.

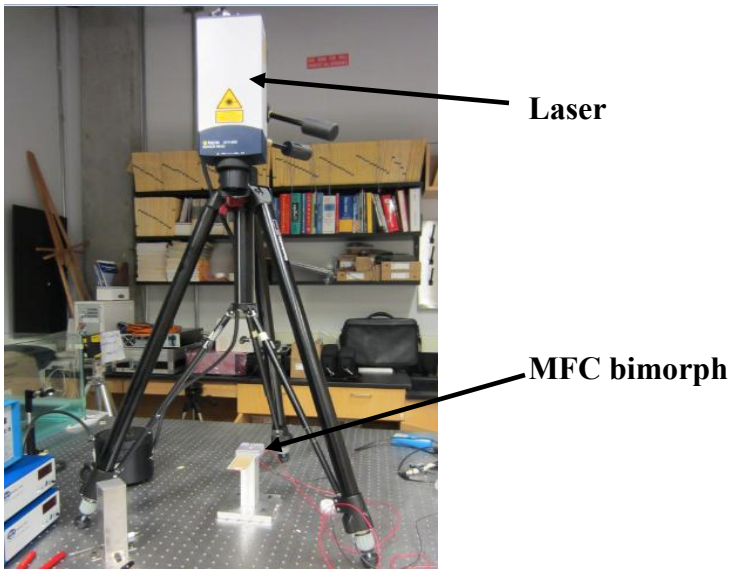

Figure 15. In-air configuration of the bimorph MFC cantilever for the measurement of its tip velocity – to – actuation voltage FRF.

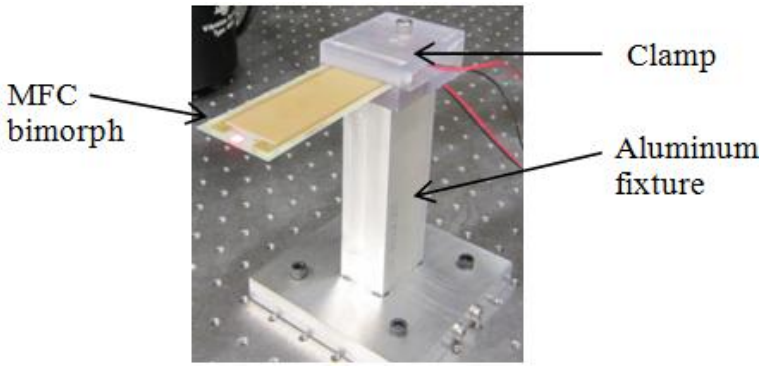

Figure 16. Close-up view showing the measurement point of vertical laser on the MFC bimorph propulsor.

Table 2. Geometric and structural properties of the piezoelectric bimorph (*L*: overhang length; *b*: total width; *h*: total thickness; *D*: flexural rigidity; m_s: structural mass per length).

L [mm]	*b* [mm]	*h* [mm]	*D* [N.m^2]	m_s [kg/m]
90.2	35.0	0.67	0.0171	0.065

4.2 Setup for underwater tip velocity FRF and mean thrust measurements

The experimental setup used for the underwater tip velocity and thrust measurements is shown in Fig. 17a. As shown in Fig. 17b, the MFC bimorph is fixed with the same clamp in the underwater experiments. Laser (1) measures the tail tip velocity under dynamic actuation while Laser (2) measures the head displacement (constrained by an aluminum cantilever) through a small mirror that makes a 45^o angle with the horizontal plane, as shown in Fig. 17c. The elastically constrained mean head displacement is correlated to the mean thrust as described in the next section. Note that both laser signals (velocity and displacement) are divided by the refractive index of water ($n = 1.333$) in the underwater experiments [43]. Attention is also given

to avoid the capturing of undesired interface (aquarium glass) reflection by slightly tilting the laser sensor head.

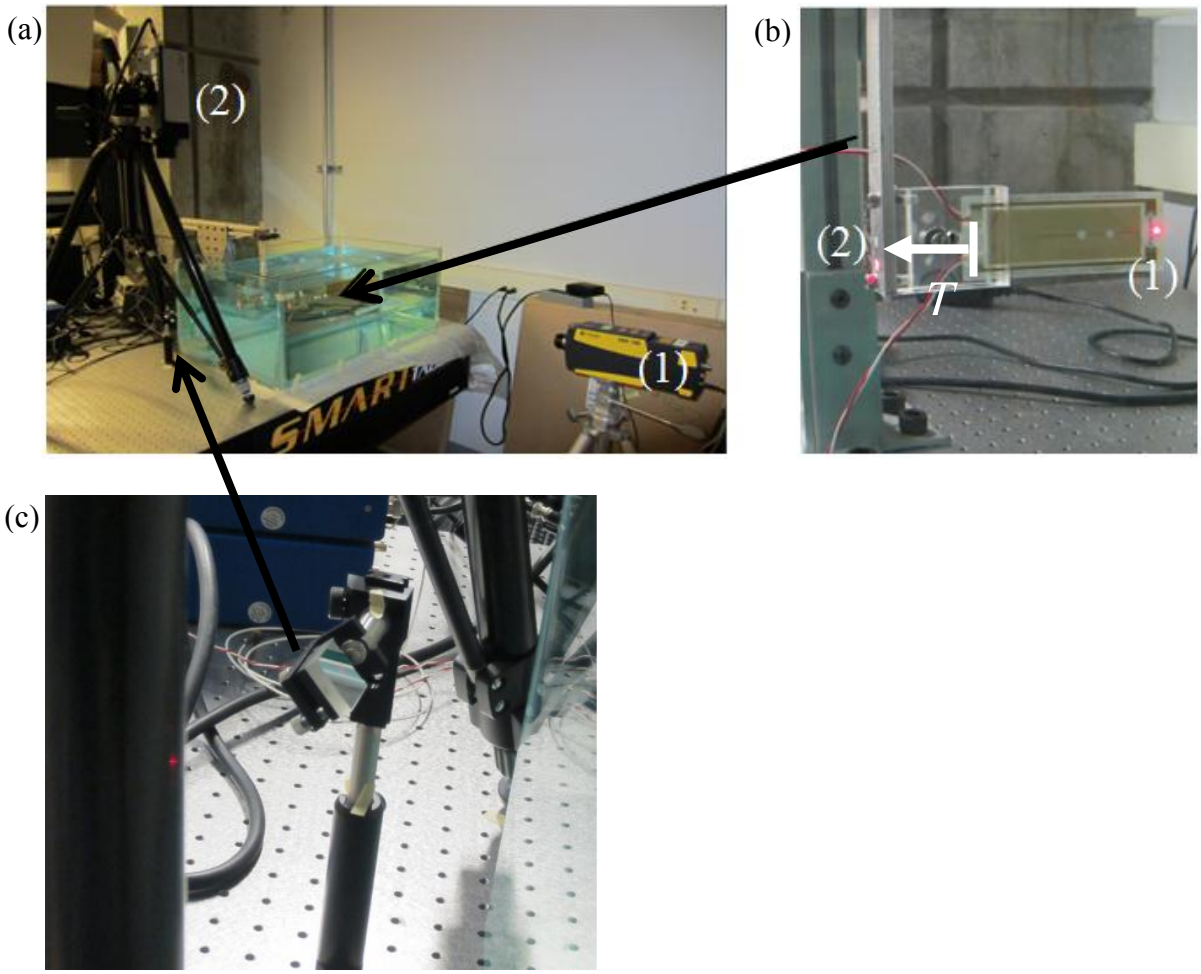

Figure 17. (a) Experimental setup used for thrust measurement of a bimorph propulsor in quiescent water: Laser (1) measures the transverse tip velocity while Laser (2) measures the head displacement through a 45^{o} mirror; (b) close-up view showing the measurement points of Lasers (1) and (2) on the MFC bimorph propulsor; (c) close-up view showing the small mirror that makes a 45^{o} angle with the horizontal plane.

4.3 Setup for calibration of the thrust measurement

The setup employed for mean thrust measurement is similar to the one used by Erturk and Delporte [43]. The MFC bimorph and its clamp are fixed at the tip of a horizontally located aluminum beam which functions as a *transducer cantilever* along with a vertically pointing laser vibrometer used in the displacement measurement mode (Fig. 18a). This laser vibrometer employed for measuring the head displacement corresponds to Laser (2) in the underwater experiments (Fig. 17a). The purpose of the in-air setup shown in Fig. 18a is to relate the thrust caused by actuation in the underwater experiments to the deflection of the aluminum transducer cantilever.

It is assumed that the mean thrust resultant (T) of the bimorph propulsor (in the underwater experiments) acts through the center of its head, causing the deflection of δ at the location of the reflector for Laser (2) in the underwater arrangement given by Fig. 18a. Different values of small masses (from 1 to 20 grams) are gradually located at the center of the top surface to emulate the mean thrust (Fig. 18b). The vertically pointing laser measures the resulting deflection at the reflector, which is employed to obtain the thrust-displacement calibration curve shown in Fig. 18c.

It is important to note that the underwater fundamental resonance frequency of transducer cantilever (in the presence of the MFC bimorph) is sufficiently higher than the underwater actuation frequencies of interest, which is checked by impact hammer testing (not discussed here). Moreover, the hydrostatic pressure effects cancel out, leaving only the hydrodynamic resultant. Therefore, in the underwater experiments, the tip deflection of the transducer cantilever is mainly due to the dynamics of the MFC bimorph propulsor [43] so that the mean head displacement value can be employed to calculate the mean thrust based on the in-air calibration.

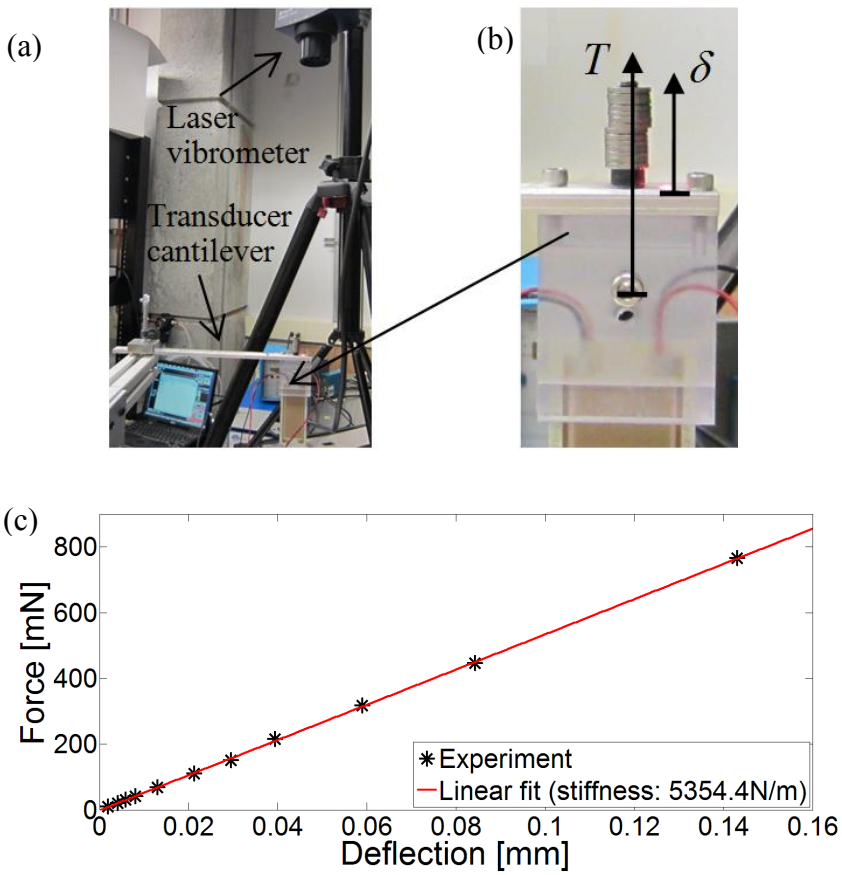

Figure 18. (a) Setup used for the thrust-displacement calibration experiment with the MFC bimorph, its clamp, and the transducer cantilever; (b) close-up view showing the point of applied loads at the center of MFC bimorph and the deflection measurement point; (c) linear calibration curve with the calculated linear stiffness (T/δ) value.

4.4 Thrust measurement procedure

The frequency range covered in the underwater thrust measurements is 0.5-15 Hz with a fine increment of 0.25 Hz in the 6-8 Hz range (resonance region) and a relatively coarse increment of 0.5 Hz outside the resonance region. Three time-domain head displacement measurements are taken at each frequency (pre-actuation, actuation, and post-actuation [43]) while the tip velocity in the transverse direction is measured simultaneously. The reference point

is calculated as the average of the pre-actuation and post-actuation values. Based on the previously discussed calibration (Section 4.3), the mean thrust is a linear function of the mean displacement of the aluminum cantilever. This mean displacement is the difference between the mean values of the *actuation* displacement and the *reference* point. From this mean displacement, the mean thrust is extracted using the linear calibration curve in Fig. 18c.

CHAPTER 5

RESULTS AND DISCUSSION

5.1 Parameter identification from in-air velocity FRF

Low-voltage harmonic input (of 0.5 V amplitude) is applied to the MFC bimorph for the frequency range of 5-70 Hz with an increment of 0.05 Hz. Figure 19 exhibits the experimentally measured tip velocity – to – actuation voltage FRF and the model prediction using Eq. (13) for the linear actuation regime of the bimorph. The fundamental in-air resonance frequency is 35.5 Hz. The in-air damping ratio (attributed to structural losses for small oscillations) is identified as $\zeta_s = 0.02$ while the identified electromechanical coupling in the physical coordinates (see Eq. (1)) is $\vartheta = 23.03\mu$Nm/V . The modal electromechanical coupling that depends on the in-air eigenfunction due to Eq. (10) is $\theta = 8.878\times10^{-3}$ N/(Vkg$^{1/2}$) .

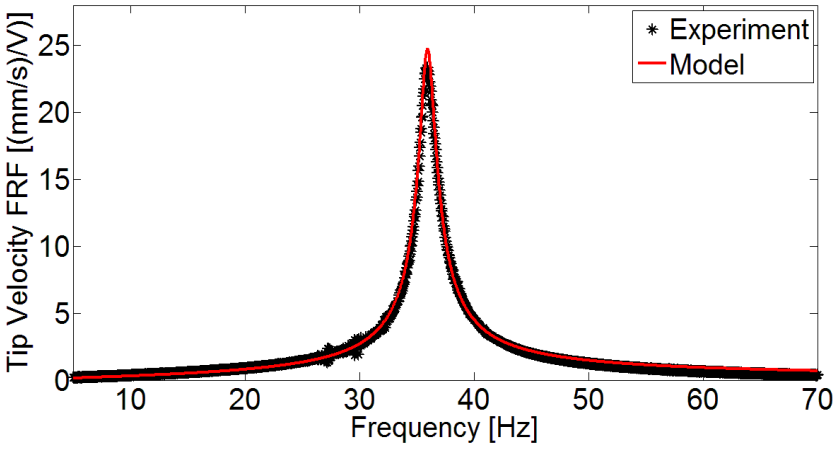

Figure 19. Measured and calculated in-air tip velocity – to – actuation voltage FRFs of the MFC bimorph in its linear actuation regime (peak-to-peak voltage input: 1 V).

5.2 Prediction of the underwater velocity FRF

Next, the MFC bimorph is immersed in water (as depicted in Fig. 17) along with its clamp and aluminum fixture used in thrust calibration (Fig. 18). Low-voltage harmonic actuation (0.5 V amplitude) is applied to the MFC bimorph for the frequency range of 2-15 Hz with an increment of 0.05 Hz. The fundamental underwater resonance frequency is measured as 8.7 Hz.

According to Eq. (22), the total underwater damping ratio is due to the structural and hydrodynamic damping effects. Equations (15) and (17) yield $\zeta_h = 0.0119$ and $\mathrm{Re} \cong 19430$, and eventually, from Eq. (22), one obtains $\zeta_w = 0.0319$. The electromechanical coupling in the physical coordinates is the same as the one obtained from in-air vibration test $(\vartheta = 23.03 \mu\text{N-m/V})$ while the modal electromechanical coupling becomes $\theta = 2.325 \times 10^{-3}$ N/(Vkg$^{1/2}$) due to Eq. (10) in which the eigenfunction is normalized according to Eq. (25). Therefore, one can predict the underwater tip velocity FRF using Eq. (27) as shown in Fig. 20.

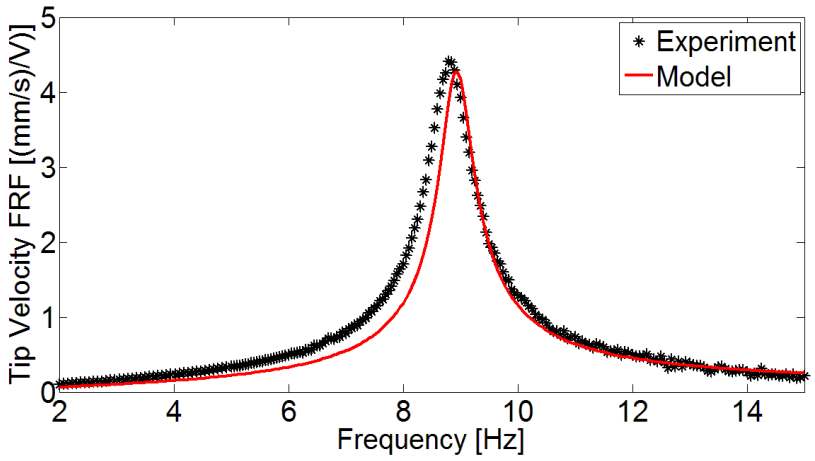

Figure 20. Measured and calculated underwater tip velocity – to – actuation voltage FRFs of the MFC bimorph in its linear actuation regime (peak-to-peak voltage input: 1 V).

The agreement between the experimental measurement and theoretical prediction is very good in the linear actuation regime of the bimorph. Equation (26) predicts the underwater resonance frequency as 8.8 Hz with an error of 1.1 % relative to the experimental value (8.7 Hz). Both the total underwater damping and natural frequency are predicted in terms of the in-air dynamics and fluid properties with good accuracy considering several assumptions stated in Section 3.1.2. Expectedly, the linear model predictions would fail under high actuation voltage levels due to geometric and electroelastic nonlinearities [88-90]. Under high actuation voltage (peak-to-peak voltage input: 200 V to 800 V), the identified electromechanical coupling term ($14 \sim 17 \mu$N-m/V) becomes smaller than the linear case (23.03μN-m/V). Modeling of MFC dynamics under high voltage actuation and incorporation of hydrodynamic effects [93] in such a nonlinear model are of interest for future work.

Here we will only show the values for the correction term in nonlinear hydrodynamic function Θ, which are identified from experiment directly. The underwater modeling use the same electromechanical coupling identified from the corresponding in-air experiments.

Table 3. Identified values for the correction term of hydrodynamic function in its nonlinear actuation regime (peak-to-peak voltage input: 200 V to 800 V).

Peak-to-peak Voltage [V]	Re ($\Delta\Gamma$)	Im ($\Delta\Gamma$)
200	0.01	0.136
400	0.01	0.21
600	0.23	0.25
800	0.26	0.276

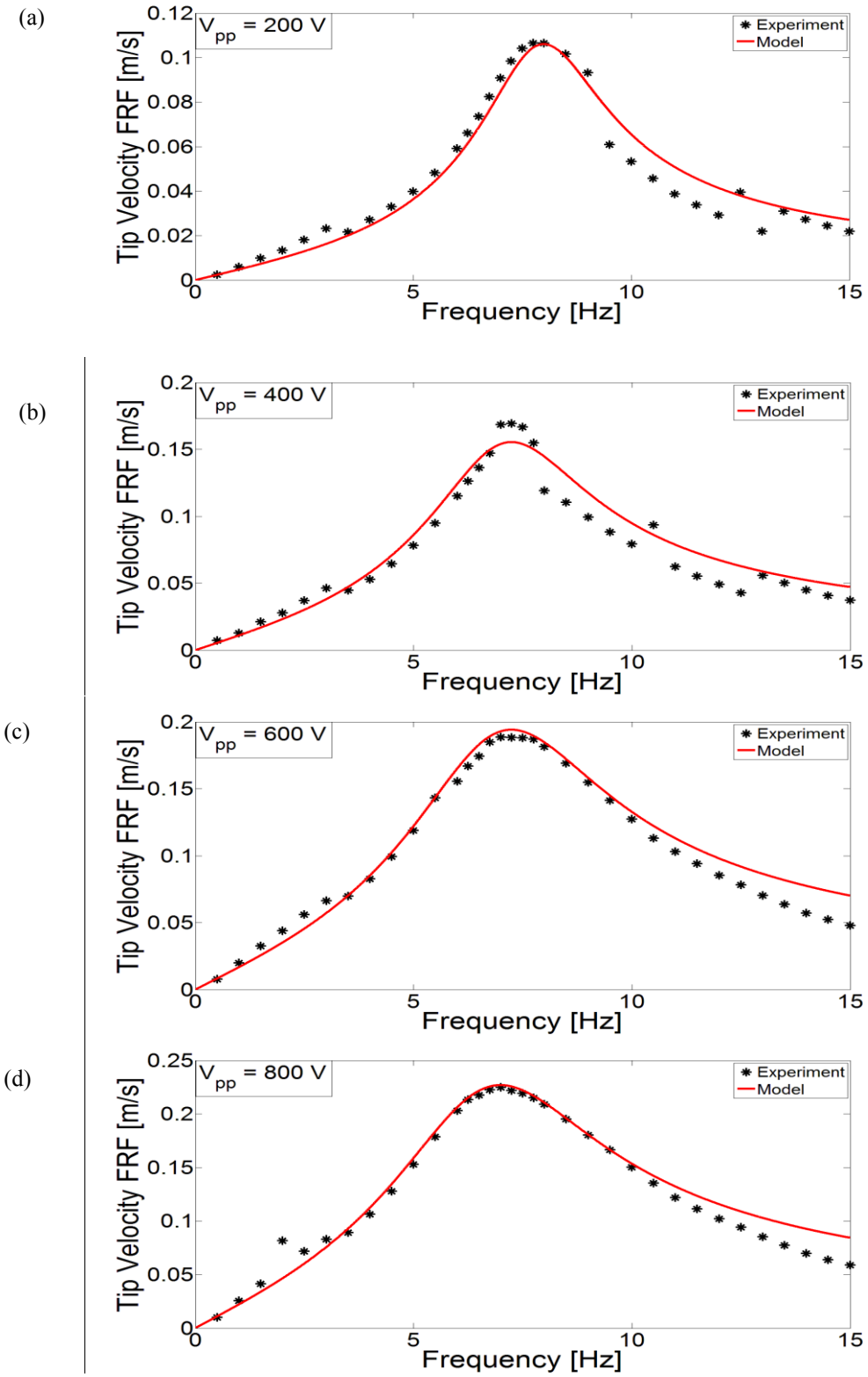

Figure 21. Measured and calculated underwater tip velocity – to – actuation voltage FRFs of the MFC bimorph in its nonlinear actuation regime (peak-to-peak voltage input: 200 V to 800 V).

From the Table 3, we can observe that the nonlinear effect increase with the vibration amplitude. Here we can also see that Sader's hydrodynamic function does not work well when the vibration amplitude is large, as mentioned before. In addition, this simple correction hydrodynamic term is just a preliminary approximation. The real nonlinear model should be much more complicate due to other nonlinear factors, such as geometric and electroelastic nonlinearities. A more comprehensive nonlinear modeling for underwater MFC vibration under high voltage actuation will be the future work.

5.3 Mean thrust and tip velocity correlation for different actuation voltage levels

The experimental tip velocity and mean thrust measurements for the peak-to-peak actuation voltage levels of 200 V, 400 V, 600 V, and 800 V are shown in Figs. 22a and 22b, respectively. Clearly, there is a direct correlation between these two independent measurements since the thrust level increases with increasing tip velocity. It should be noted that these high actuation voltage levels fall into the nonlinear regime due to the electroelastic, geometric, and dissipative nonlinear effects. The softening nonlinearity (resulting in the shifting of the resonance frequency to the left) with increased actuation input is a typical behavior of piezoelectric cantilevers under high voltage actuation [89].

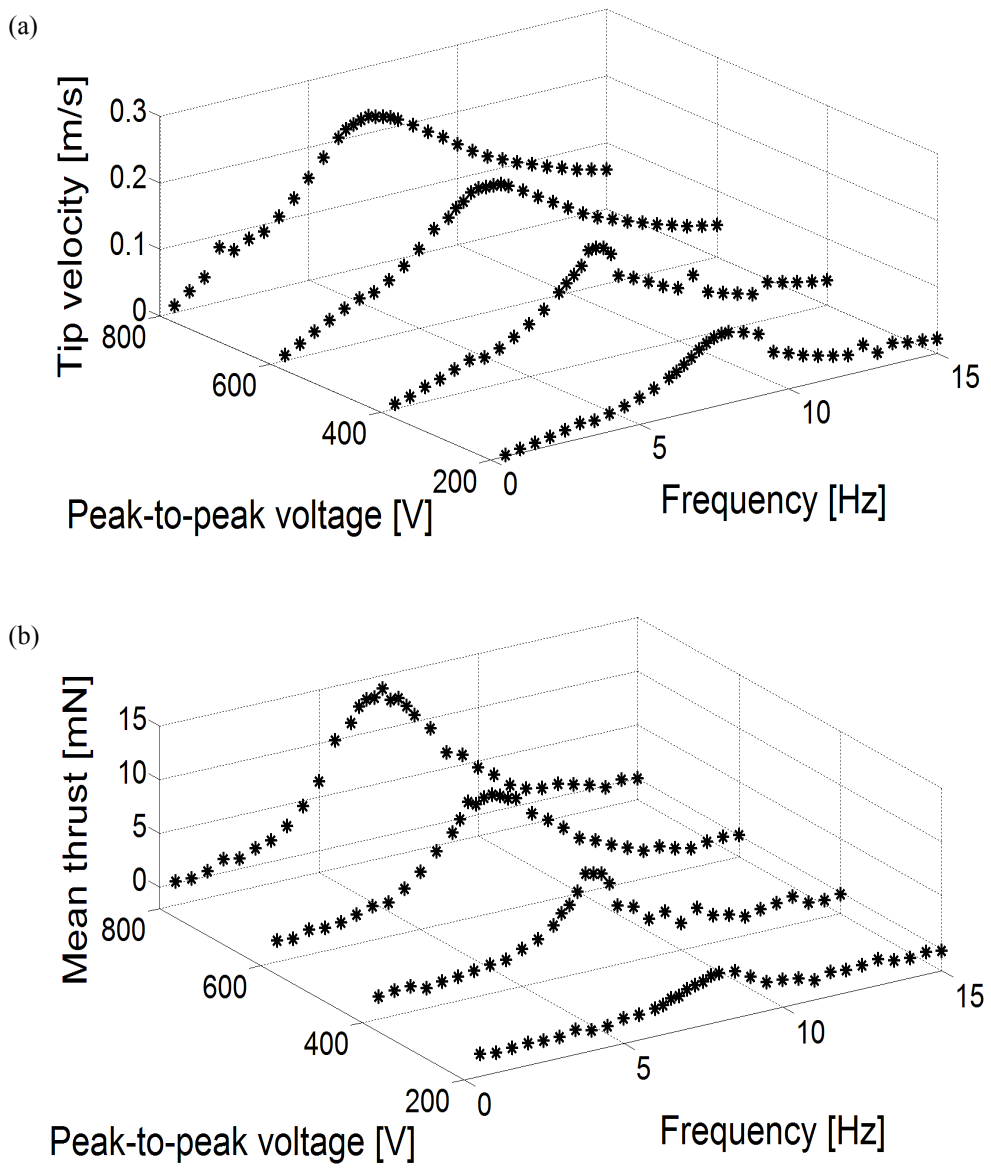

Figure 22. Experimental (a) tip velocity and (b) mean thrust curves for four different peak-to-peak voltage levels: 200 V, 400 V, 600 V, and 800 V.

Using Eq. (31) resulting from Lighthill's theory for the quiescent water condition, one can estimate the thrust curves in terms of the tip velocity and the virtual mass. These predictions are shown in Figs. 23a-d for four different actuation voltage levels. Note that, particularly in Fig. 23a (which is the lowest voltage case among these four measurement sets), the frequencies away

from the resonance region are prone to noise effects in the measurements due to low thrust resultant (caused by low displacement). Based on Figs. 23a-d, it can be concluded that the reduced form of Lighthill's theory [10-12] for quiescent water can predict the mean thrust in terms of the tip velocity with good accuracy for this specific MFC bimorph.

(a)

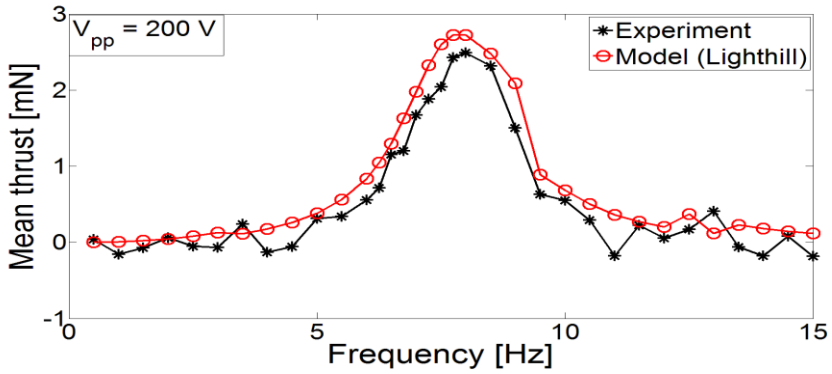

(b)

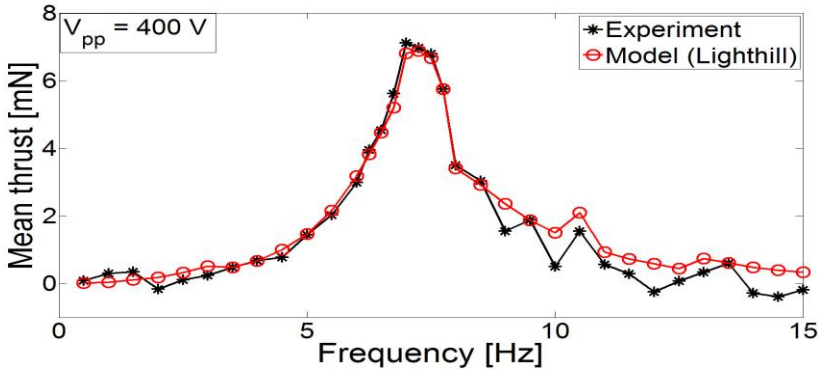

(c)

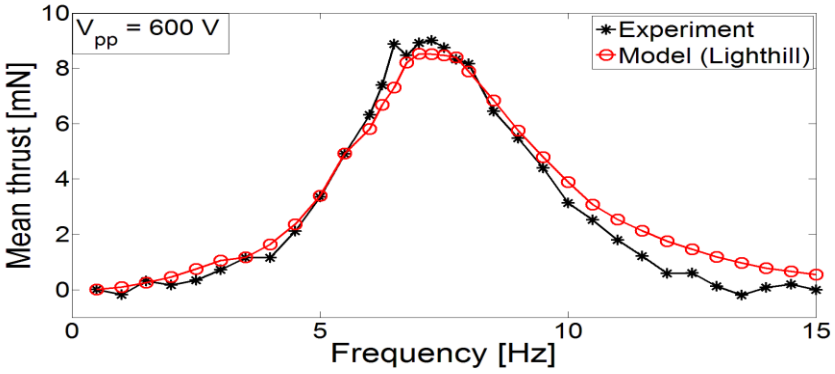

(d)

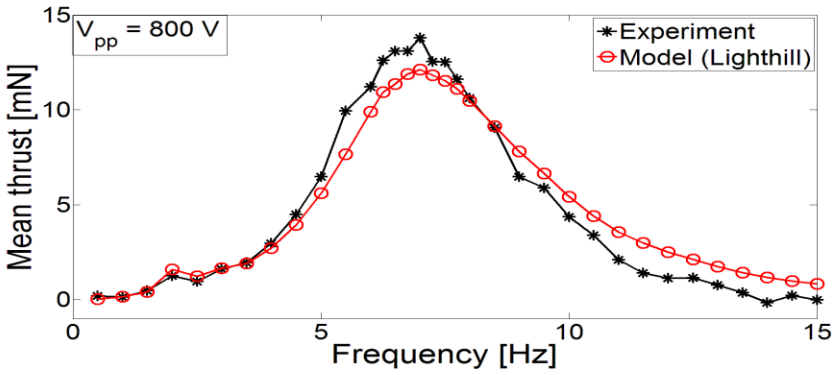

Figure 23. Measured and predicted thrust curves for the peak-to-peak voltage inputs of (a) 200 V, (b) 400 V, (c) 600 V, and (d) 800 V.

Even though this reduced form of Lighthill's slender body theory does correlate the tip velocity to mean thrust with good accuracy for this specific MFC bimorph, it should be note that no complete theory is currently available for estimating the thrust production of vibrating cantilever beams in placid environment [13]. Many IPMC-based robotic fish groups utilized the Lighthill's slender theory based on the assumption that "a body is considered slender if its cross-sectional area of the body changes slowly along its length" [26, 29, 102]. Lighthill's slender fish concept is just an approximation method, which comes from slender body theory on flow about airships. Theoretically, this approximation will be better when the aspect ratio of the actuator is larger [102]. However, in practice, the IPMC-based robotic fish's aspect ratio for actuator is just around 2 to 3 when they utilized Lighthill's slender fish concept [26, 29]. Similarly, the aspect ratio is just 2.6 in this specific MFC bimorph. In the future, more different aspect ratios of MFC bimorph will be test to further evaluate the availability of this reduced Lighthill's slender body theory for MFC bimorph thrust estimation.

5.4 Identification of the thrust coefficient

Recently, Abdelnour *et al* [103] utilized Particle Image Velocimetry (PIV) technology to identify the thrust coefficient. PIV provides a direct way of analyzing the water flow around fish body. These days planar PIV has been used to measure the mean flow field induced by vibrating IPMC cantilever strips in quiescent aqueous environments. This mean flow field information can then be utilized for IPMC thrust estimation [13]. They also numerically analyzed the flow of an unbounded incompressible Newtonian fluid generated by a rectangular cantilever IPMC strip [103]. They found that the IPMC thrust increases approximately linearly as the square of the modified Reynolds number Re_L , shown as below:

$$\mathrm{Re}_L = \frac{\omega \delta_p L}{\upsilon} \tag{32}$$

$$\beta = \frac{\delta_p}{L} \tag{33}$$

$$C_\tau = \frac{\tau}{\frac{1}{2}\rho_w \omega^2 \delta^2 L} = \frac{\tau}{\frac{1}{2}\frac{\rho_w \upsilon^2 \mathrm{Re}_L^2}{L}} \tag{34}$$

where υ is the kinematic viscosity of water that is equal to μ/ρ_w , δ_p is the peak tip displacement, β is the relative peak tip displacement, τ is the thrust per unit width of the actuator, C_τ is the thrust coefficient. The peak tip speed can be expressed as $\omega\delta_p$.

Comparing the equation (31) with (34), we would find that they both share some similarities since Re_L is linearly related to the fin tip velocity. Therefore, the estimated thrust is approximately proportional to the square of Re_L or the fin tip velocity, as shown below in equation (35) and Fig. 24.

$$T \cong \frac{1}{2} m_v \overline{\left(\frac{\partial w}{\partial t} \right)^2} \Bigg|_{x=L} = \frac{\pi \rho_w b^2}{8} \overline{\left(\frac{\partial w(L,t)}{\partial t} \right)^2} = \frac{\pi \rho_w b^2 \upsilon^2}{16 L^2} \mathrm{Re}_L^2 \qquad (35)$$

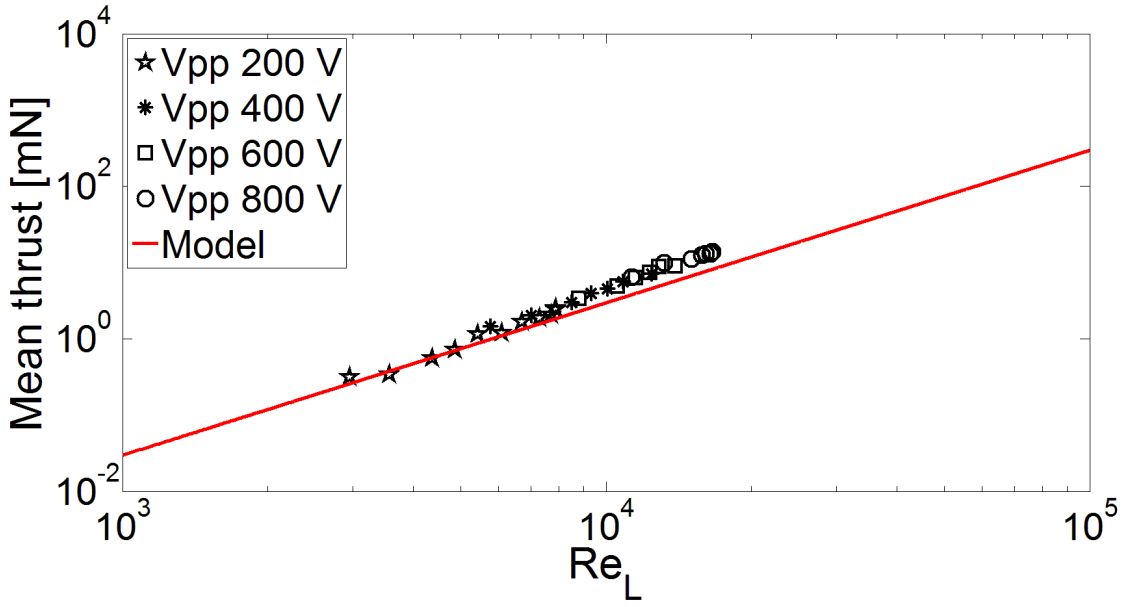

Figure 24. Experimental mean thrust versus the Reynolds number Re_L for the four different high peak to peak voltages.

Table 4. The peak tip displacement and the relative peak tip displacement for the four different high peak to peak voltages.

Vpp (volt)	δ_p [mm]	β
200	2.21	0.025
400	3.83	0.042
600	4.36	0.048
800	6.48	0.072

Similar to the IPMC thrust experiment result in [103], the measured MFC mean thrust increases as Re_L^2 and is not significantly influenced by the relative peak tip displacement β. The thrust coefficient C_τ can be calculated by substituting Equation (31) into (34), which is a constant for these four high voltage actuations.

$$C_\tau = \frac{\pi b}{8L} \approx 0.1524 \tag{36}$$

Although thrust estimation in the present work has been observed similar trends with IPMC thrust estimation experiments using PIV, both the classic Lighthill's slender body theory and PIV-based method still need to be test in more different cases (aspect ratio, peak tip displacement, material, etc.) for further evaluation.

CHAPTER 6

PIEZOELECTRIC ROBOTIC FISH PROTOTYPE

A separate bimorph propulsor is fabricated for the free-locomotion experiments. An embedded power and control system is designed for this prototype, which can generate high input voltage for the MFC bimorph propulsor. As shown in Fig. 25a, this system consists of two 9 V batteries, a microcontroller (ATmega 128), a wireless device (XBee 1mW Wire Antenna - Series 1 (802.15.4)) and a PCB amplifier (AMD2012-CE3) specially designed for the MFC actuator [45]. In order to obtain smooth sinusoidal voltage for the MFC bimorph, a low pass filter is added to filter out the high frequency noise from the pulse width modulation (PWM) signals. The detailed schematic of the actuation system is shown in Fig. 25b.

(a)

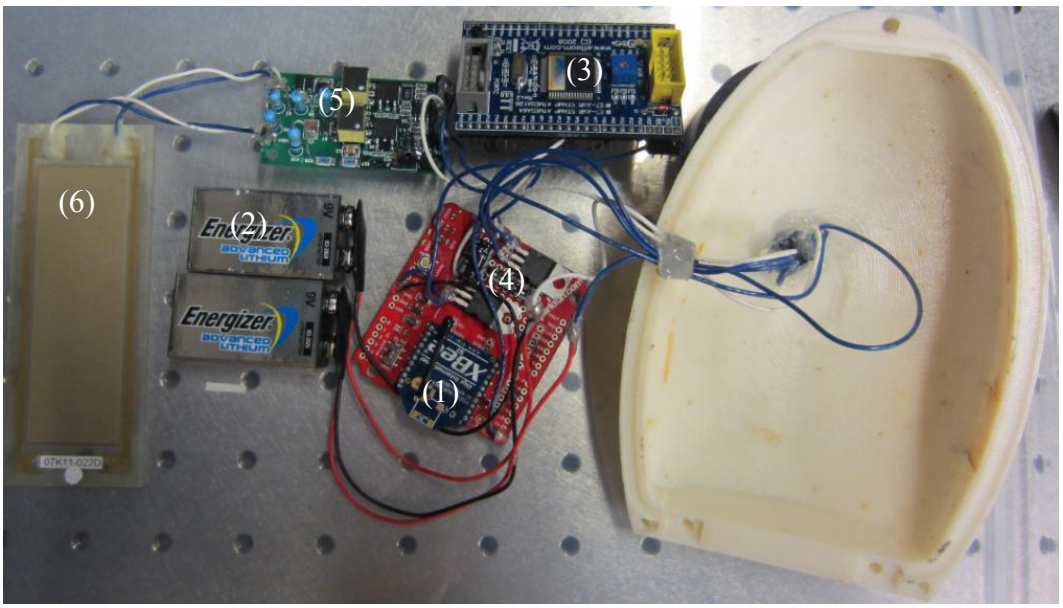

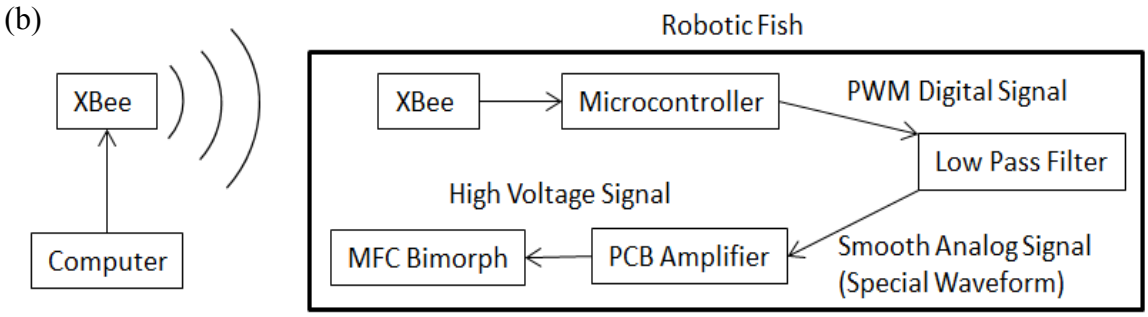

Figure 25. (a) Components for the untethered robotic fish system: (1) XBee radio; (2) 9V batteries; (3) microcontroller; (4) low pass filter and voltage regulators; (5) voltage amplifier; (6) MFC bimorph; and (b) electronic schematic of the robotic fish system.

Despite the advantages of MFCs due to large dynamic actuation stresses, structural flexibility, silent operation, and wide frequency range of effective performance, the requirement of high voltage input limits its application in free locomotion for robotic fish development. To the best of our knowledge, untethered free locomotion using piezoelectric robotic fish (without external power supply) does not exist in the literature [2-5]. High voltage input requirement and low strain output are the two shortages of piezoelectric transduction limiting the application of piezoelectric structures for robotic fish development.

In order to overcome the shortage of low strain in piezoelectric robotic configurations, various magnification mechanisms were proposed by others, as shown in [2-4]. However, the magnification component that is employed for creating larger vibration amplitudes might create noise and cause additional energy loss. In order to satisfy the high input voltage requirement, research groups used wire connection to power piezoelectric robotic fish, which restricts the free-locomotion capability [2-5].

In the next two section (Sec 6.1 and 6.2), I will describe how to overcome these two shortages (low strain and high input voltage) to fabricate the first free-locomotion piezoelectric robotic fish without extra magnification mechanic structure and external power supply.

6.1 Fabrication of the MFC bimorph fin

MFC is utilized to deal with the shortage of low strain in piezoelectric robotic configurations. MFC is a relatively new smart material, which developed at the NASA Langley Research Center in the last decade [44]. It exhibits high efficiency in size, reduced energy consumption, and noiseless performance. In addition, MFCs offer large dynamic stresses in bending actuation as well as high performance for both low-frequency and high-frequency applications.

The bimorph is made of two hydrophobic M8528-P1 [45] MFC laminates with no separate substructure layer other than the Kapton and epoxy layers of the MFCs. A vacuum bonding process is employed by using high shear strength epoxy to assemble the piezoelectric laminates (this process is described elsewhere [104]). These two customized hydrophobic MFC samples are parallel connected in our bimorph propulsor circuit to generate larger vibration amplitude.

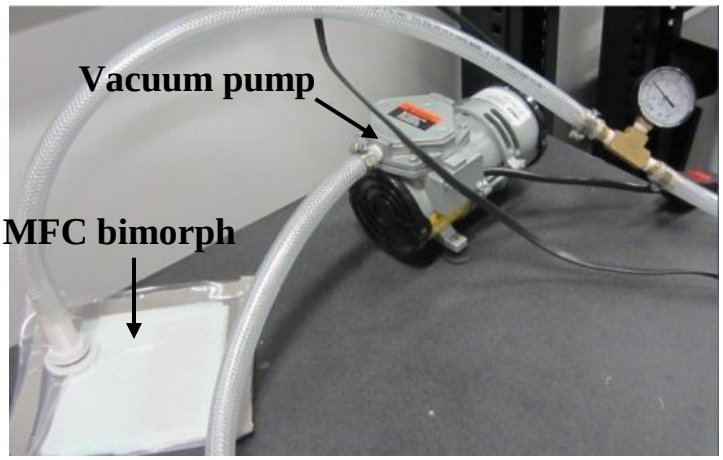

Figure 26. Set up for MFC bimorph propulsor fabrication.

6.2 Embedded power system

In order to enable tether-free locomotion of the MFC-based robotic fish, a portable power system has to be designed to generate the high voltage for MFC bimorph actuation. The general maximum output voltage level for ATMega 128 microcontroller is just around 5 volts, which is much lower than the requirements for MFC actuation. A special designed PCB amplifier (AMD2012-CE3) is utilized in our power system [45], which is able to generate high voltage from -500 V to 1500 V according to the control input signal from 0 V to 5 V. This PCB amplifier only requires 12 V input voltage supply. Therefore, the portable power system can be made by simply using two 9 V batteries, a microcontroller (ATmega 128), a special designed PCB amplifier and the corresponding voltage regulators, as shown in Fig. 27. These two 9 V batteries can support the continuous operation of the system for almost 30 minutes. Lithium ion battery is selected as the power source since it is lightweight and has high power density. The power consumption of the overall electronic system is around 3 to 5 W. The current amplitude and average power plots for MFC bimorph vibration under different frequencies and actuation voltages are shown in Fig. 28. As we can see from Fig. 28b, the average power of MFC bimorph around its fundamental mode is less than 1 W (sinusoidal peak-to-peak voltage of 800 V). The overall power consumption of the robotic fish can still be further reduced by optimizing the circuit design in the future.

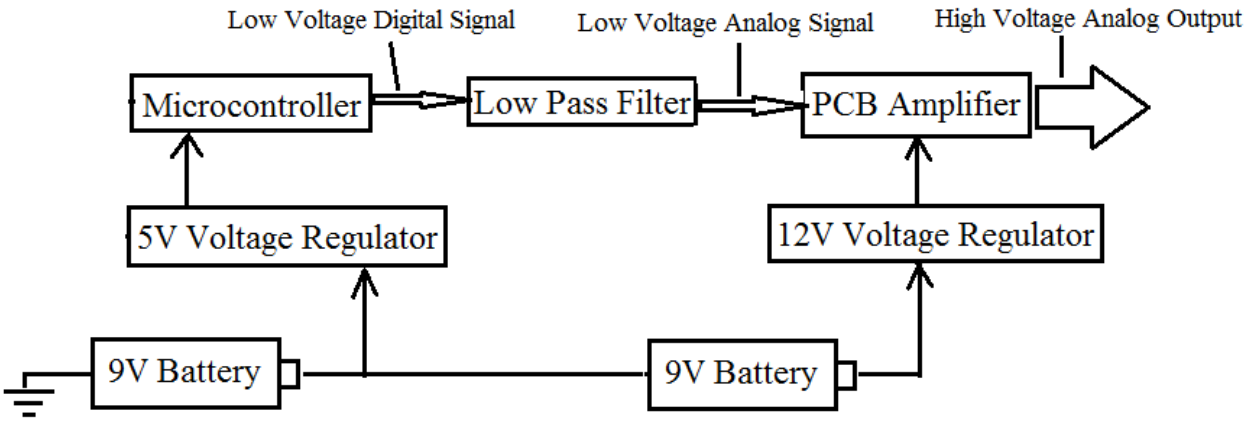

Figure 27. Power system for the robotic fish

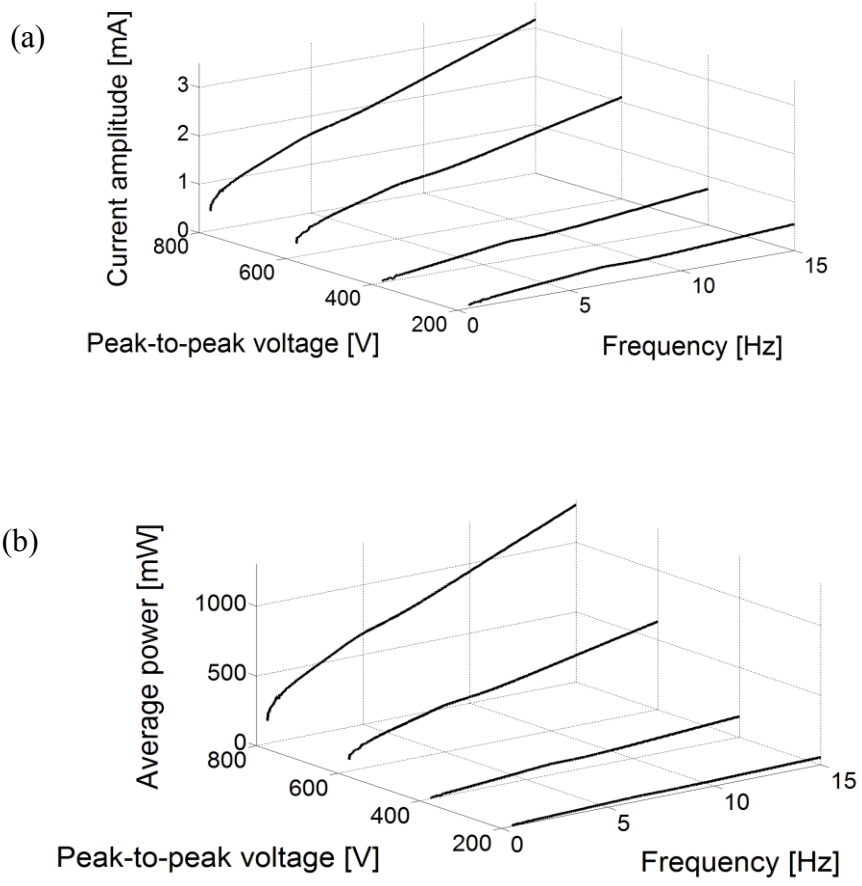

Figure 28. Experimental (a) current amplitude and (b) average power curves for four different peak-to-peak voltage levels: 200 V, 400 V, 600 V, and 800 V.

6.3 Embedded wireless control system for maneuverability

In order to provide sinusoidal high voltage for the MFC bimorph, the microcontroller is programmed to generate a special waveform by PWM. Specifically, 0 V input signal generates -500 V output; 2.5 V input signal generates 0 V output; 5 V input signal generates 1500 V output. These values are the voltage limits of MFCs without depolarization [45]. An example is given in Fig. 29 for the case of generating a sinusoidal peak-to-peak voltage of 800 V at 10 Hz using the PCB amplifier.

The microcontroller is able to generate various waveforms by its PWM function. Therefore, this power system can provide the high voltage sinusoidal output (up to 2000 V peak-to-peak) for the MFC bimorph propulsor. The frequency, mean voltage, and amplitudes of the PCB amplifier output signal can be controlled by adjusting the rate and duty cycle of the PWM signals. The swimming speed is easily controlled through PCB amplifier output signal frequencies and amplitudes. In addition, turning speed and direction are controlled by setting different values for the amplitudes A_1 and A_2 to enable maneuverability. When $A_1 = A_2$, it swims straight forward. And it turns left or right, when $A_1 \neq A_2$, as shown in Fig. 29b.

Wireless control is performed through serial communication. Commands are sent by a laptop computer through a USB connected XBee Explorer. An XBee module inside the robotic fish body receives the commands and transfers them to the microcontroller, which can change the PWM waveform. Therefore, wireless communication controls the swimming speed and direction of the robotic fish by setting the rate and duty cycle of the PWM, which affect the vibration frequency and amplitude of the MFC propulsor.

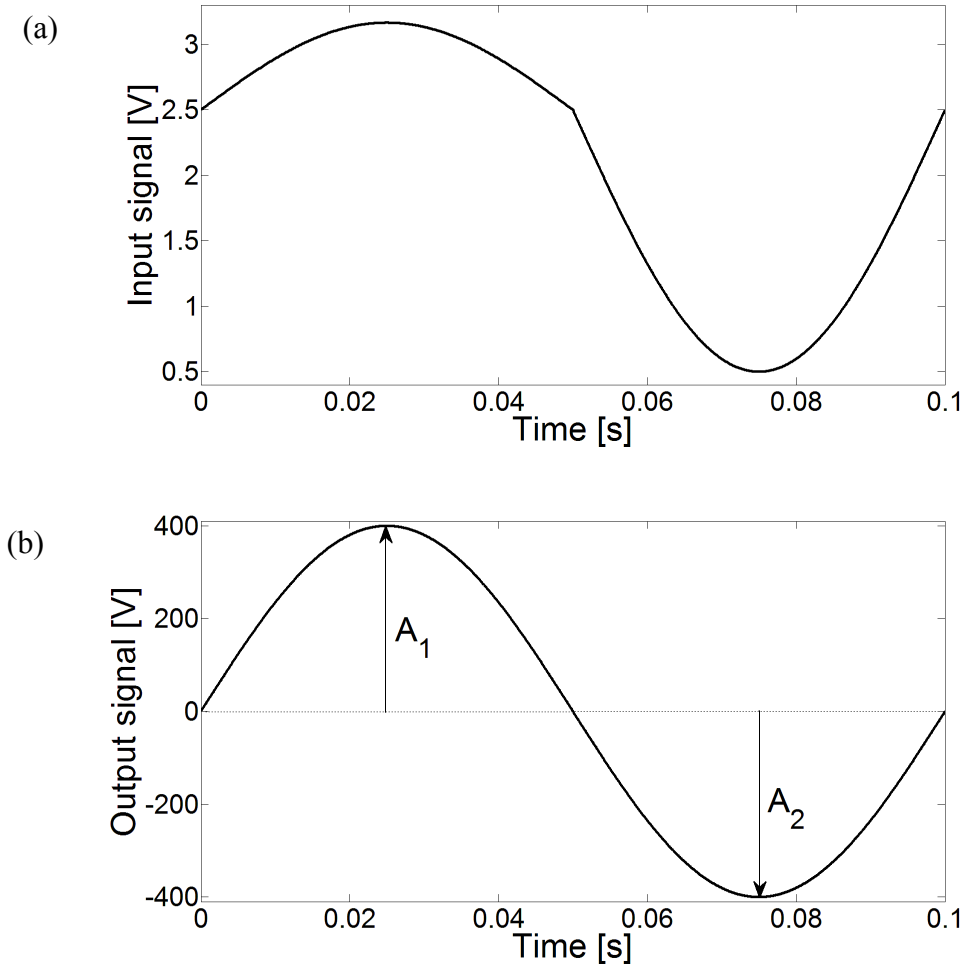

Figure 29. (a) Input and (b) output signals of the PCB amplifier to generate a sinusoidal peak-to-peak actuation voltage of 800 V at 10 Hz.

6.4 Prototype fabrication procedure

At first, all the electronic components are test in a fish body made by foam, as shown in Fig. 30. Foam is employed for this first test prototype due to low cost and easy handling. This foam prototype is purely made (cut) by hand, which serves as a preliminary platform to test the electronic components, such as power system and control system, etc. Two side fins are attached

to the robotic fish body to enhance roll and pitch stability. In this hand-made prototype, no counter weight is used since the side fins are enough to stabilize the body.

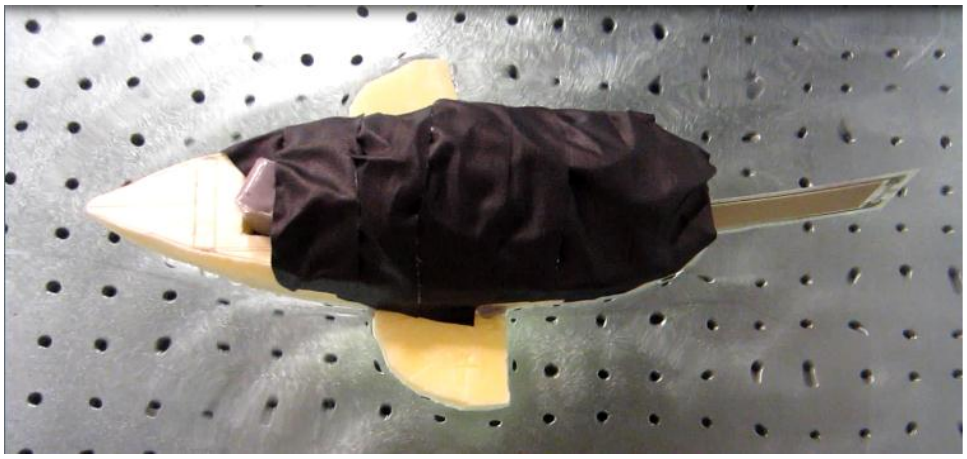

Figure 30. Preliminary robotic fish prototype for free locomotion.

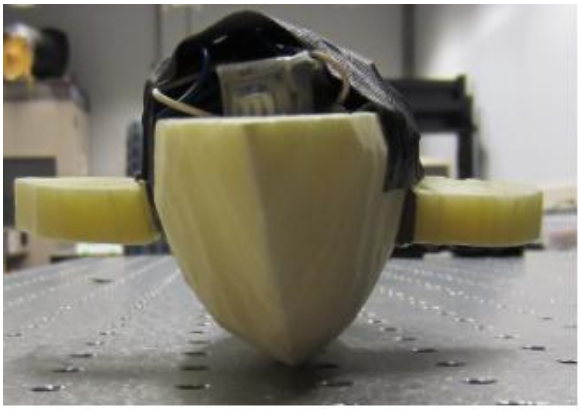

Figure 31. Imperfections of the hand-made foam robotic fish prototype.

Table 5. Components of the hand-made foam robotic fish prototype (units are in grams).

MFC bimorph		11
Power and control system	Two batteries	64.8
	Microcontroller	18
	PCB amplifier	13.4
	Battery connectors	4
	Two voltage regulators	3.6
	Capacitor	1
	Wires	6
	Switch	0.8
Robotic fish body (foam, clamp, glue, and waterproof tapes, etc.)		50.8
Counter weight		0
Total mass of the robotic fish		173.4

The control system and power system has been successfully test in this hand-made foam prototype. However, as shown in Fig. 31, this hand-made foam body has many imperfections: (1) This hand-cut surface is coarse and not strictly regular, which will increase the drag force; (2) The two side fins increase the contact surface or drag force, which slow down the swimming speed; (3) The electronic components are cover by a tape, which is not well waterproof.

A picture of the new piezoelectric robotic fish prototype is shown in Fig. 34. The robotic fish body shell was designed in SolidWorks and then printed on a Fused Deposition Modeling (FDM) machine. This created an Acrylonitrile Butadiene Styrene (ABS) plastic shell, that when

printed is buoyant in water. This printed body shell is much smoother and more regular than the hand-made one, which is good for reducing the drag force.

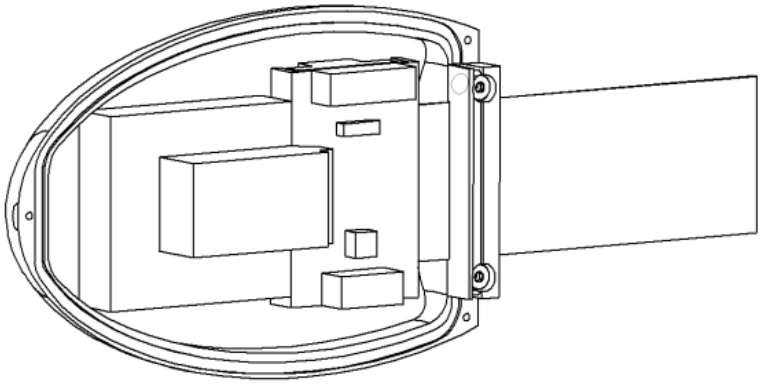

Figure 32. SolidWorks drawing for the printed robotic fish prototype (inner view).

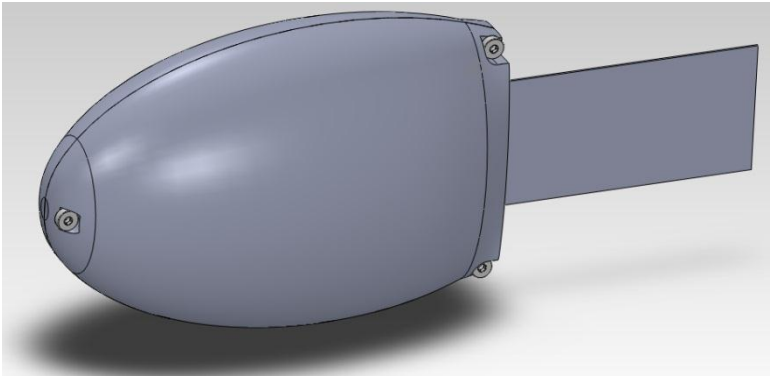

Figure 33. SolidWorks drawing for the printed robotic fish prototype (outside view).

Figure 34. The printed robotic fish prototype.

In order to increase swimming speed and reduce contact surface, the two side fins are removed in this printed prototype. Counter weight is implemented at the bottom of the interior hull to enhance roll and pitch stability instead. In addition, the fish body was designed to provide a waterproof enclosure for the electronics components. An O-ring was integrated into the rim to ensure the interior of the fish stayed dry in order to protect the electronics. Another water-proof package is utilized to further protect the electronic components, especially the high voltage power system.

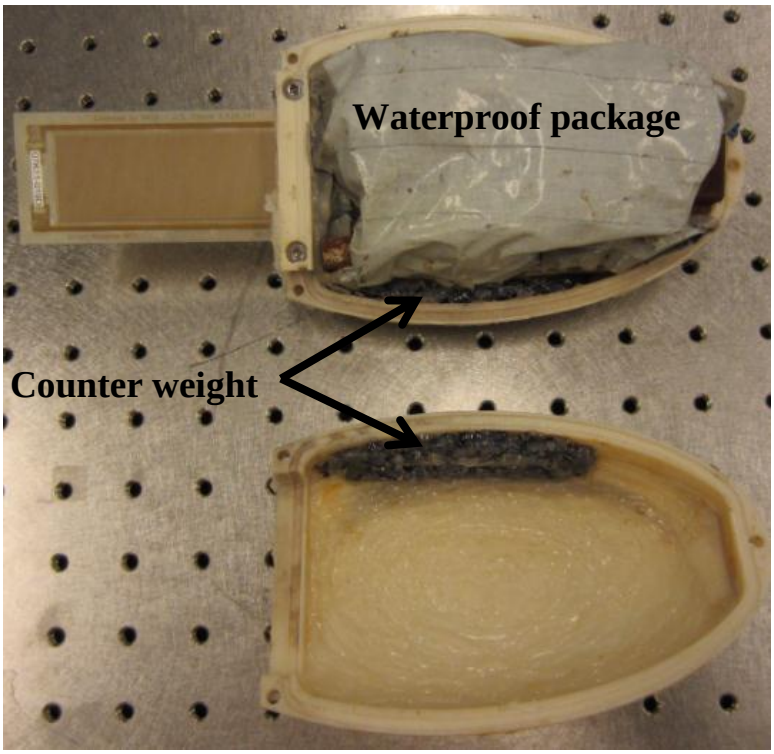

Figure 35. Internal configuration of the printed piezoelectric robotic fish prototype.

This prototype was intended merely for proof of concept, as the large volume (and hence buoyant force) requires a significant amount of counterweight. The total weight of the prototype

is 541.8 grams which has more detailed mass analysis in Table 6. Further improvements can be realized by increasing the actuation voltage to a larger level with a DC offset (since MFC laminates have asymmetric voltage limits: -500 V to 1500 V).

Table 6. Components of the printed piezoelectric robotic fish prototype (units are in grams).

MFC bimorph		11
Power, wireless and actuation system	Two batteries	64.8
	Microcontroller	18
	PCB amplifier	13.4
	XBee module	16.9
	Battery connectors	4
	Two voltage regulators	3.6
	Capacitor	1
	Wires	6
	Switch	0.8
Robotic fish body (shell, clamp, glue, and waterproof tapes, etc.)		168.8
Counter weight		233.5
Total mass of the robotic fish		541.8

6.5 Free locomotion tests

The free swimming test is performed in a glass tank (20 inch width, 30 inch long, and 15 inch height). A camera (Canon PowerShot ELPH 300 HS) is employed to take video for the free swimming of the piezoelectric robotic fish. The Xbee signal would penetrate the water just a few

centimeters so the robotic fish is not test deeply underwater. The wireless communication is used for testing the change of speed and direction continuously during swimming. As mentioned before, the swimming speed and direction can be adjusted by setting the rate and duty cycle of the PWM, which affect the vibration frequency and amplitude of the MFC propulsor.

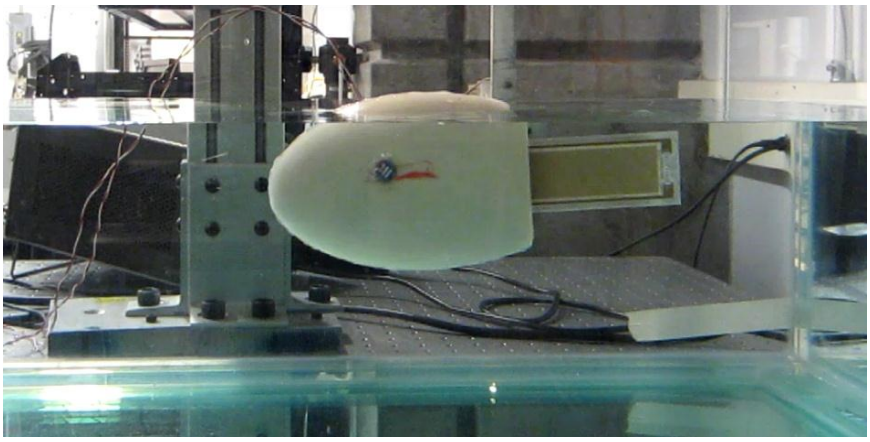

Figure 36. Side view of the untethered piezoelectric robotic fish.

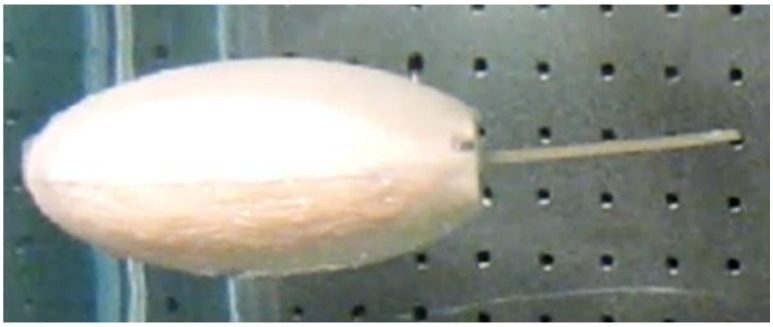

Figure 37. Top view of the untethered piezoelectric robotic fish. Maximum swimming speed under peak-to peak actuation voltage of 1000 V at 5 Hz is approximately 7.5 cm/s.

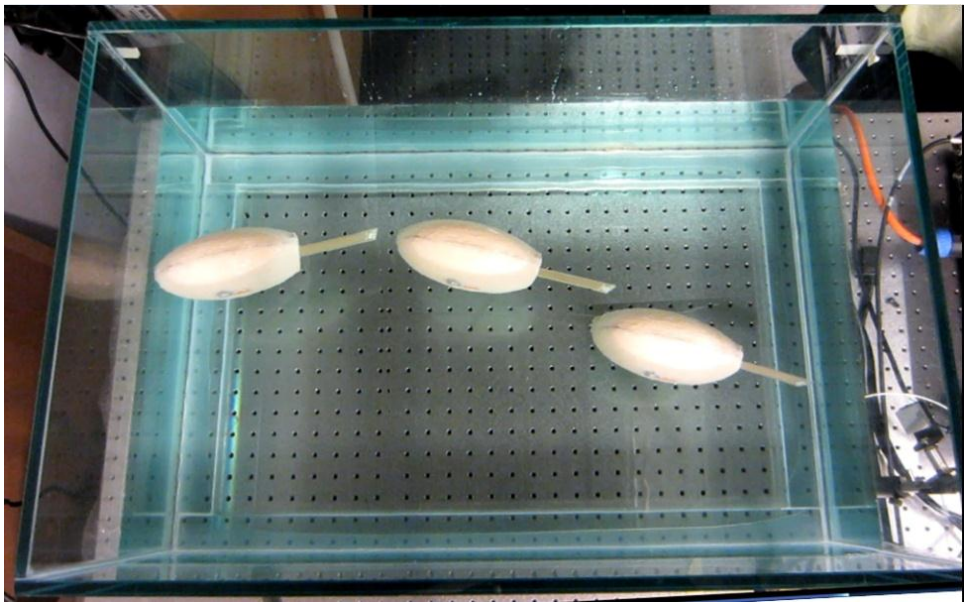

Figure 38. Combined motion capture (Top view). Wireless communication is employed to change the speed and direction during swimming test.

Figure 39. Combined motion capture for straight forward, turn left, and turn right swimming motion.

6.6 Comparison with other smart material-based and motor-based robotic fish

The swimming speed for a peak-to-peak actuation voltage of 1000 V at 5 Hz is measured as 7.5 cm/s. This is equivalent to almost 0.3 body length per second and it compares favorably with several smart actuator-based aquatic robots reported in the literature (including wired ones) [16][*] even though the present prototype excludes the caudal fin extension and volumetric optimization. The caudal fin extension is known to improve not only the thrust amplitude but also the bandwidth of effective excitation frequencies [43].

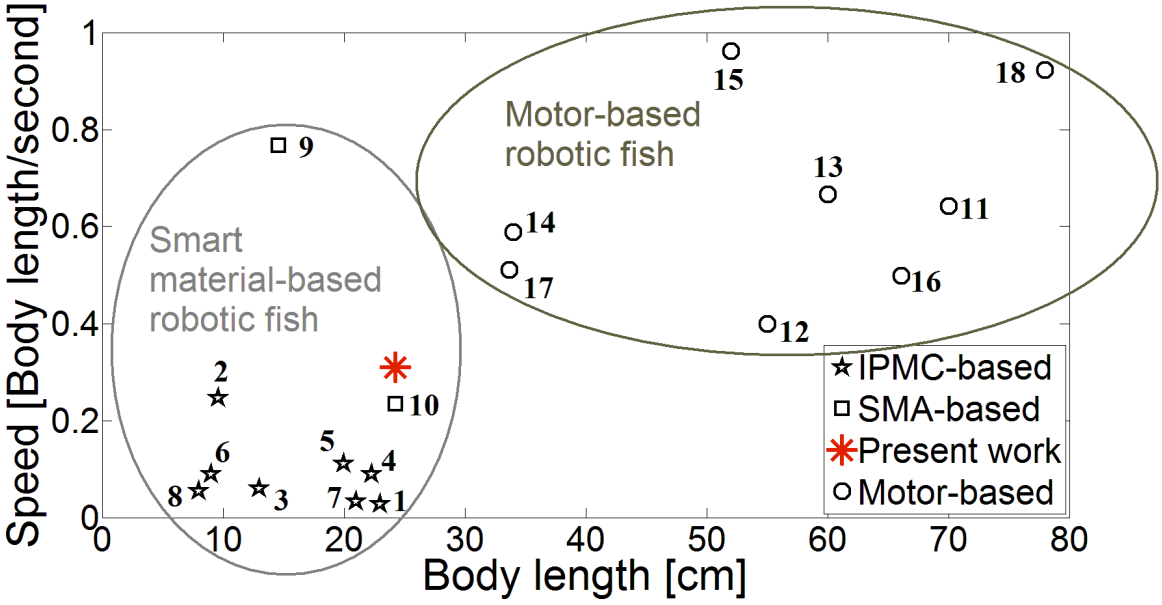

Figure 40. Comparison of IPMC, SMA, Motor and Piezoelectric based untethered robotic fish. (speed per body length vs. robot length)

As we can see from the table 1 and Fig. 40, our preliminary robotic fish (without caudal fin) is in the intersection of IPMC and motor based robotic fish. Motor based robotic fish

[*] The piezoelectric-based robot [37] reviewed by Chu et al. [3] was powered through wires.

generally have larger speed per body length than smart material based ones. One important reason is that smart material based robotic fish are still in the stage of early development, compared to the long history development of motor based robotic fish. However, smart material based robotic fish still show their advantages in body size, noise reduction and energy efficiency. Comparing with untethered IPMC-based robotic fish, the present MFC robotic fish show its advantage in speed per body length.

CHAPTER 7

CONCLUSIONS AND RECOMMENDATIONS FOR FUTURE WORK

7.1 Conclusions

Biomimetic aquatic robotics using Macro-Fiber Composite (MFC) piezoelectric bimorphs is investigated theoretically and experimentally for fish-like locomotion. In-air and underwater dynamics of an MFC bimorph cantilever is modeled for small amplitude bending vibrations under piezoelectric actuation. Hydrodynamic effects are introduced to the electroelastic model based on Sader's work [6] on cantilevers vibrating in fluids for a wide range of Reynolds numbers. Lighthill's slender-body theory [10-12] is used to predict the thrust output in quiescent water by reducing Lighthill's mean thrust expression to the quiescent water condition. In-air and underwater experiments are conducted for model validation and for the characterization of a bimorph propulsor. The hydrodynamic effects added to the electroelastic in-air model successfully predict the underwater dynamics for small oscillations. However, for future work, nonlinear electrohydroelastic modeling (combining nonlinear electroelastic dynamics [88-90] with nonlinear hydrodynamic effects [93]) is required to predict the dynamics of the propulsor for large oscillations and under high electric field levels.

The underwater experiments resulted in mean thrust levels as high as 14 mN around 7 Hz for the peak-to-peak actuation voltage of 800 V using a 90 mm x 35 mm x 0.67 mm cantilever in the absence of a caudal fin extension [32] (note that the MFCs can perform without depolarization up to peak-to-peak actuation voltage of 2000 V). Fish-like propulsors made of MFCs can therefore successfully imitate thrust levels of biological fish [105].

A battery-powered robotic fish prototype that incorporates a microcontroller and a printed-circuit-board (PCB) amplifier is developed and tested in free locomotion. A swimming speed of 0.3 body length per second (7.5 cm/s swimming speed for 24.3 cm body length) is achieved for a non-optimized main body–propulsor combination, which is substantially better performance as compared to IPMC-based robotic fish. This swimming speed of the first prototype can be improved substantially by increasing the actuation voltage, optimizing the volume, and using a caudal fin extension. The untethered prototype introduced in this work serves to exploit the potential benefits of piezoelectric material in fish-like propulsion.

7.2 Recommendations for future work

7.2.1 Nonlinear electrohydroelastic modeling

The agreement between the experimental measurement and theoretical prediction is very good in the linear actuation regime of the bimorph. For nonlinear case (high actuation voltage), we only identify the values for correction term in nonlinear hydrodynamic function from experiment. This simple hydrodynamic correction term is just a preliminary approximation following the recent work [93, 94]. A complete nonlinear treatment is more sophisticated than just incorporation the hydrodynamic effects due to other nonlinear factors, such as geometric and electroelastic nonlinearities.

Future work should build a more comprehensive model for the nonlinear actuation regime for MFC bimorph so that the thrust under high actuation voltage can be estimated directly from the in-air velocity FRF. Finite element simulation packages can be helpful in determining the correction term in nonlinear hydrodynamic function [93].

7.2.2 Evaluation of the thrust estimation method for different types of MFC bimorphs

In this research, the estimated thrust of MFC bimorph matches well with the measured ones. However, the theory for estimating thrust production of vibrating cantilever beams with finite dimensions is still controversial [13]. Even though many IPMC-based robotic fish groups utilized the Lighthill's slender theory based on the assumption that "a body is considered slender if its cross-sectional area of the body changes slowly along its length" [26, 29, 102], a few others found that the reduced Lighthill's slender body theory approximately overpredicts the thrust by one order of magnitude for their specific IPMC thrust experiment.

Lighthill's slender fish concept is just an approximation method, which originates from the slender body theory of aerodynamics. Theoretically, this approximation is better justified when the aspect ratio of the actuator is larger [102]. In the future, different aspect ratios of MFC bimorphs should be tested to further evaluate the validity of Lighthill's slender body theory for MFC bimorph thrust estimation.

7.2.3 Swimming speed estimation

In the thesis, the thrust estimations and experiments are performed for the quiescent water condition. The maximum speed we have obtained in this experiment is 7.5 cm/s under a peak-to-peak actuation voltage of 1000 V at 5 Hz. Future work can focus on building additional experiment set up to estimate the drag force under different swimming speed, as shown in Fig. 13. More swimming tests under different applied voltages and frequencies can be conducted to characterize the relationship between hydrodynamic thrust and swimming speed with relation to the drag force.

7.2.4 Improvement of the preliminary piezoelectric robotic fish prototype

In this first free swimming piezoelectric robotic fish, the electronic components are obtained from different companies, such as microcontroller module, XBee module, and the PCB amplifier. These electronic components have redundant parts, which can be removed to reduce the volume of the main body. In the next prototype, miniaturization of the electrical devices will be performed to reduce the total volume of the piezoelectric robotic fish. Almost half of the weight is due to the counter weight in the present configuration (Table 6). If we can largely reduce the total volume, the contact surface and drag force can be largely reduced, which is very beneficial to save power and increase swimming speed.

APPENDIX A

SLENDER BODY THEORY (LIGHTHILL) [102]

In this theory, we consider swimming movements which enable the fish to stay still in water flowing with velocity U in the x-direction. The inviscid flow around the fish is investigated.

The slender fish in the stream is considered as "stretched straight" when it is held stationary in a standard position such that no resultant normal force acts on any cross-section. When the fish is stretched straight the cross-section of its surface S at a distance x downstream from the nose will be denoted by S_x.

We suppose now that in swimming the cross section S_x receives a displacement $h(x,t)$ from the stretched straight position, in the z-direction, so that the displacement is at right angles to the direction of locomotion and varies both with position and time. Then on slender-body theory the flow can be regarded as compounded of

(i) The steady flow around the stretched straight body;

(ii) The flow due to the displacements $h(x,t)$

For the flow component (ii), we observe that a cross-section S_x moves, relative to the fluid flowing past it with velocity U, at a velocity

$$V(x,t) = \frac{\partial h}{\partial t} + U\frac{\partial h}{\partial x} \tag{A.1}$$

And that, locally, the body shape differs little from that of an infinite cylinder C_x whose cross-section is S_x all the way along. Accordingly, to the slender-body approximation, the flow

component (ii) near S_x is identical with the two-dimensional potential flow that would result from the motion of the cylinder C_x through fluid at rest with velocity $V(x,t)$.

We suppose now that this flow has momentum

$$\rho V(x,t)A(x) \tag{A.2}$$

per unit length of cylinder, where ρ is the water density. In the usual terminology, $\rho A(x)$ is the "virtual mass m_v" of the cylinder C_x per unit length for motions in the z-direction.

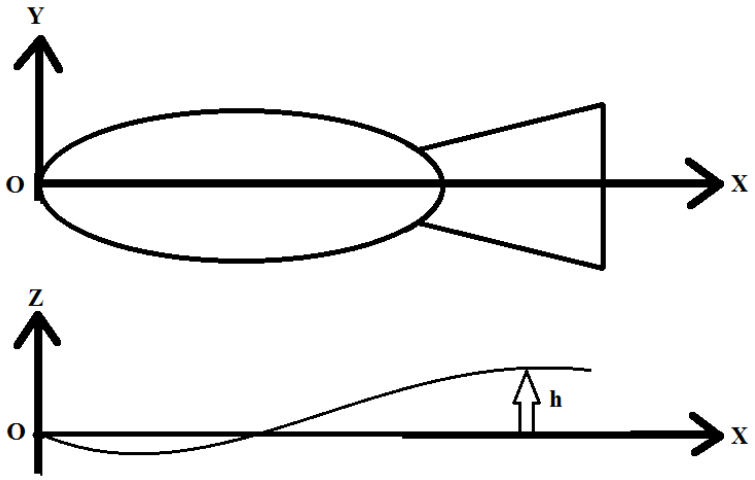

Figure A.1. Shape and motion of the fish.

To obtain the instantaneous lift per unit length of fish, $L(x,t)$, which is the force in the z-direction on the cross-section S_x, we observe that this must be equal and opposite to the rate of change of momentum of the fluid passing S_x; that is,

$$L(x,t) = -\rho\left(\frac{\partial}{\partial t} + U\frac{\partial}{\partial x}\right)\{V(x,t)A(x)\} \tag{A.3}$$

And then we can write down the rate, W, at which the fish does work by making displacements $h(x,t)$ in the direction in which these lift forces act; that is

$$W = -\int_0^l \frac{\partial h}{\partial t} L(x,t)dx = \frac{\partial}{\partial t}\left\{\rho\int_0^l \frac{\partial h}{\partial t} VA(x)dx - \frac{1}{2}\rho\int_0^l V^2 A(x)dx\right\} + \rho U[\frac{\partial h}{\partial t} VA(x)]_0^l \qquad \text{(A.4)}$$

The mean over a long time of the time-derivative in this last expression is zero.

$$\frac{\partial}{\partial t}\left\{\rho\int_0^l \frac{\partial h}{\partial t} VA(x)dx - \frac{1}{2}\rho\int_0^l V^2 A(x)dx\right\} = 0 \qquad \text{(A.5)}$$

For the final term $\rho U\left[\frac{\partial h}{\partial t} VA(x)\right]_0^l$, we have $A(0) = 0$, but because the fish has a tail $A(l)$ is non-zero---at least on the approximation of assuming a straight trailing edge, which makes $A(l)$ equal to the area of the circle with the trailing edge as diameter. Hence, (A. 4) gives for the mean rate of working by the fish

$$\overline{W} = \rho UA(l)\left\{\overline{\frac{\partial h}{\partial t}(\frac{\partial h}{\partial t} + U\frac{\partial h}{\partial x})}\right\}_{x=l} \qquad \text{(A. 6)}$$

$$\overline{W} = \rho UA(l)\left\{\overline{\frac{\partial h}{\partial t}\left(\frac{\partial h}{\partial t} + U\frac{\partial h}{\partial x}\right)}\right\}_{x=l} = (\rho VA)U\frac{\partial h}{\partial t} \quad \text{since} \quad V(x,t) = \frac{\partial h}{\partial t} + U\frac{\partial h}{\partial x} \qquad \text{(A. 7)}$$

This value can be interpreted physically as the mean of the product of the lateral velocity $\frac{\partial h}{\partial t}$ of the tail trailing edge with the rate of shedding $(\rho VA)U$ of lateral momentum behind the trailing edge, on the argument that rate of working equals velocity times rate of change of momentum.

On the other hand, the rate of shedding of kinetic energy of lateral fluid motions is $(\frac{1}{2}\rho V^2 A)U$. If, now, we subtract the mean value of this from the mean rate of working $\overline{W}$, we should obtain the rate of working available for producing the mean thrust, say, $\overline{P}$; this rate is $\overline{P}U$.

To sum up,

$$\overline{W} - \frac{1}{2}\rho \overline{V}^2 AU = \overline{P}U \tag{A. 8}$$

Hence by (6) the mean thrust is

$$\overline{P} = \frac{1}{2}\rho A(l)\left\{\overline{\left(\frac{\partial h}{\partial t}\right)^2} - U^2\overline{\left(\frac{\partial h}{\partial x}\right)^2}\right\}_{x=l} = \frac{1}{2}m_v\left\{\overline{\left(\frac{\partial h}{\partial t}\right)^2} - U^2\overline{\left(\frac{\partial h}{\partial x}\right)^2}\right\}_{x=l} \tag{A. 9}$$

where m_v is the virtual mass density at $x = L$,

REFERENCES

1. Barrett, D., M. Grosenbaugh, and M. Triantafyllou, *The optimal control of a flexible hull robotic undersea vehicle propelled by an oscillating foil.* Proceedings of the 1996 Symposium on Autonomous Underwater Vehicle Technology, 1996: p. 1-9.
2. Fukuda, T., et al., *Steering mechanism and swimming experiment of micro mobile robot in water.* Micro Electro Mechanical Systems - Ieee Proceedings, 1995, 1995: p. 300-305.
3. Heo, S., et al., *Effect of an Artificial Caudal Fin on the Performance of a Biomimetic Fish Robot Propelled by Piezoelectric Actuators.* Journal of Bionic Engineering, 2007. **4**(3): p. 151-158.
4. Wiguna, T., et al., *Design and Experimental Parameteric Study of a Fish Robot Actuated by Piezoelectric Actuators.* Journal of Intelligent Material Systems and Structures, 2009. **20**(6): p. 751-758.
5. Ming, A.G., et al., *Development of Underwater Robots using Piezoelectric Fiber Composite.* Icra: 2009 Ieee International Conference on Robotics and Automation, Vols 1-7, 2009: p. 3435-3440.
6. Sader, J.E., *Frequency response of cantilever beams immersed in viscous fluids with applications to the atomic force microscope.* Journal of Applied Physics, 1998. **84**(1): p. 64-76.
7. Van Eysden, C.A. and J.E. Sader, *Frequency response of cantilever beams immersed in viscous fluids with applications to the atomic force microscope: Arbitrary mode order.* Journal of Applied Physics, 2007. **101**(4).
8. Chon, J.W.M., P. Mulvaney, and J.E. Sader, *Experimental validation of theoretical models for the frequency response of atomic force microscope cantilever beams immersed in fluids.* Journal of Applied Physics, 2000. **87**(8): p. 3978-3988.
9. Van Eysden, C.A. and J.E. Sader, *Resonant frequencies of a rectangular cantilever beam immersed in a fluid.* Journal of Applied Physics, 2006. **100**(11).
10. Lighthill., M.J., *Hydromechanics of Aquatic Animal Propulsion.* Annual Review of Fluid Mechanics, 1969. **1**: p. 413-&.
11. Lighthill., M.J., *Aquatic Animal Propulsion of High Hydromechanical Efficiency.* Journal of Fluid Mechanics, 1970. **44**(Nov11): p. 265-&.
12. Lighthill., M.J., *Large-Amplitude Elongated-Body Theory of Fish Locomotion.* Proceedings of the Royal Society of London Series B-Biological Sciences, 1971. **179**(1055): p. 125-&.
13. Peterson, S.D., M. Porfiri, and A. Rovardi, *A Particle Image Velocimetry Study of Vibrating Ionic Polymer Metal Composites in Aqueous Environments.* Ieee-Asme Transactions on Mechatronics, 2009. **14**(4): p. 474-483.
14. Bandyopadhyay, P.R., *Trends in biorobotic autonomous undersea vehicles.* Oceanic Engineering, IEEE Journal of, 2005. **30**(1): p. 109-139.
15. Roper, D., et al., *A review of developments towards biologically inspired propulsion systems for autonomous underwater vehicles.* Proceedings of the Institution of Mechanical Engineers, Part M: Journal of Engineering for the Maritime Environment, 2011. **225**(2): p. 77-96.
16. Chu, W.S., et al., *Review of biomimetic underwater robots using smart actuators.* International Journal of Precision Engineering and Manufacturing, 2012. **13**(7): p. 1281-1292.
17. Shahinpoor, M., *Conceptual Design, Kinematics and Dynamics of Swimming Robotic Structures Using Active Polymer Gels.* Active Materials and Adaptive Structures, 1992: p. 91-95.
18. Mojarrad, M. and M. Shahinpoor, *Noiseless propulsion for swimming robotic structures using polyelectrolyte ion-exchange membrane.* Smart Materials Technologies and Biomimetics - Smart Structures and Materials 1996, 1996. **2716**: p. 183-192.
19. Laurent, G. and E. Piat, *Efficiency of swimming microrobots using ionic polymer metal composite actuators.* 2001 Ieee International Conference on Robotics and Automation, Vols I-Iv, Proceedings, 2001: p. 3914-3919.
20. Kim, K.J., *Fabrication and development of electroactive ionic polymer-metal composites and their applications as smart materials.* Thermec'2003, Pts 1-5, 2003. **426-4**: p. 2249-2254.
21. Kim, B., et al., *A biomimetic undulatory tadpole robot using ionic polymer-metal composite actuators.* Smart Materials & Structures, 2005. **14**(6): p. 1579-1585.

22. Chung, C.K., et al., *A novel fabrication of ionic polymer-metal composites (IPMC) actuator with silver nano-powders.* Transducers '05, Digest of Technical Papers, Vols 1 and 2, 2005: p. 217-220.
23. Guo, S.X., et al., *Underwater swimming micro robot using IPMC actuator.* IEEE ICMA 2006: Proceeding of the 2006 IEEE International Conference on Mechatronics and Automation, Vols 1-3, Proceedings, 2006: p. 249-254.
24. Chung, C.K., et al., *A novel fabrication of ionic polymer-metal composites (IPMC) actuator with silver nano-powders.* Sensors and Actuators B-Chemical, 2006. **117**(2): p. 367-375.
25. Tan, X.B., et al., *An autonomous robotic fish for mobile sensing.* 2006 IEEE/RSJ International Conference on Intelligent Robots and Systems, Vols 1-12, 2006: p. 5424-5429.
26. Mbemmo, E., et al., *Modeling of biomimetic robotic fish propelled by an ionic polymer-metal composite actuator.* 2008 Ieee International Conference on Robotics and Automation, Vols 1-9, 2008: p. 689-694.
27. Jeon, J.H., S.W. Yeorn, and I.K. Oh, *Fabrication and actuation of ionic polymer metal composites patterned by combining electroplating with electroless plating.* Composites Part a-Applied Science and Manufacturing, 2008. **39**(4): p. 588-596.
28. de Witt, B.J. and R.J. Hugo, *A Preliminary Study of the Transition of an in-Line Pipe Vortex to Slug Flow Using Particle Image Velocimetry.* Proceedings of the Asme Fluids Engineering Division Summer Conference -2008, Vol 1, Pt a and B, 2009: p. 637-646.
29. Chen, Z., S. Shatara, and X.B. Tan, *Modeling of Biomimetic Robotic Fish Propelled by An Ionic Polymer-Metal Composite Caudal Fin.* Ieee-Asme Transactions on Mechatronics, 2010. **15**(3): p. 448-459.
30. Aureli, M., V. Kopman, and M. Porfiri, *Free-Locomotion of Underwater Vehicles Actuated by Ionic Polymer Metal Composites.* Ieee-Asme Transactions on Mechatronics, 2010. **15**(4): p. 603-614.
31. Shinjo, N. and G.W. Swain, *Use of a shape memory alloy for the design of an oscillatory propulsion system.* Ieee Journal of Oceanic Engineering, 2004. **29**(3): p. 750-755.
32. Wang, Z.L., et al., *A micro-robot fish with embedded SMA wire actuated flexible biomimetic fin.* Sensors and Actuators a-Physical, 2008. **144**(2): p. 354-360.
33. Wang, Z., et al., *Embedded SMA wire actuated biomimetic fin: a module for biomimetic underwater propulsion.* Smart Materials and Structures, 2008. **17**: p. 025039.
34. Cho, K.J., et al., *Design, fabrication and analysis of a body-caudal fin propulsion system for a microrobotic fish.* 2008 Ieee International Conference on Robotics and Automation, Vols 1-9, 2008: p. 706-711.
35. Rossi, C., et al., *Bending continuous structures with SMAs: a novel robotic fish design.* Bioinspiration & Biomimetics, 2011. **6**: p. 045005.
36. Rossi, C., et al. *A motor-less and gear-less bio-mimetic robotic fish design*. 2011. IEEE.
37. Zhang, Y.S. and G.J. Liu, *Design, analysis and experiments of a wireless swimming micro robot.* 2005 IEEE International Conference on Mechatronics and Automations, Vols 1-4, Conference Proceedings, 2005: p. 946-951.
38. Zhang, Y.S. and G.J. Liu, *Wireless micro biomimetic swimming robot based on giant magnetostrictive films.* 2005 IEEE International Conference on Robotics and Biomimetics, 2006: p. 195-200.
39. Zhang, Y.S. and G.J. Liu, *Wireless Swimming Microrobot: Design, Analysis, and Experiments.* Journal of Dynamic Systems Measurement and Control-Transactions of the Asme, 2009. **131**(1).
40. Zhang, Z., *Design and control of a fish-like robot using an electrostatic motor.* Proc. IEEE ICRA, Rome 2007, 2007.
41. Zhang, Z., M. Philen, and W. Neu, *A biologically inspired artificial fish using flexible matrix composite actuators: analysis and experiment.* Smart Materials and Structures, 2010. **19**: p. 094017.
42. Philen, M. and W. Neu, *Hydrodynamic analysis, performance assessment, and actuator design of a flexible tail propulsor in an artificial alligator.* Smart Materials and Structures, 2011. **20**: p. 094015.
43. Erturk, A. and G. Delporte, *Underwater thrust and power generation using flexible piezoelectric composites: an experimental investigation toward self-powered swimmer-sensor platforms.* Smart Materials & Structures, 2011. **20**(12).

44. Wilkie, W.K., et al., *Low-Cost Piezocomposite Actuator for Structural Control Applicaitons.* Smart Structures and Materials, 2000.
45. *Smart Material Corp.*
46. Lindsey, C.C., *Form, function and locomotory habits in fish.* Fish Physiology, 1978. **Vol. VII**: p. pp. 1–100.
47. Breder, C.M., *The locomotion of fishes.* Zoologica, 1926. **vol. 4**: p. pp. 159–256.
48. Lighthil.Mj, *Hydromechanics of Aquatic Animal Propulsion.* Annual Review of Fluid Mechanics, 1969. **1**: p. 413-&.
49. Sfakiotakis, M., D.M. Lane, and J.B.C. Davies, *Review of fish swimming modes for aquatic locomotion.* Ieee Journal of Oceanic Engineering, 1999. **24**(2): p. 237-252.
50. Leo, D.J., *Engineering analysis of smart material systems*2007, Hoboken, N.J.: John Wiley & Sons. xiv, 556 p.
51. Wallace, G.G., Spinks, G.M., Kane-Maguire, L.A.P., and Teasdale, P.R., *Conductive Electroactive Polymers: Intelligent Materials Systems*2003: Florida: CRC Press.
52. Baughman, R.H., *Conducting polymer artificial muscles.* Synthetic Metals, 1996. **78**(3): p. 339-353.
53. Madden, J.D., et al., *Fast contracting polypyrrole actuators.* Synthetic Metals, 2000. **113**(1-2): p. 185-192.
54. Alici, G. and N.N. Huynh, *Performance quantification of conducting polymer actuators for real applications: A microgripping system.* Ieee-Asme Transactions on Mechatronics, 2007. **12**(1): p. 73-84.
55. Kim, K., and Satoshi, T, *Electroactive Polymers for Robotic Applications.* 2007.
56. Alexander, P.W. and D. Brei, *Piezoceramic telescopic actuator quasi-static experimental characterization.* Journal of Intelligent Material Systems and Structures, 2003. **14**(10): p. 643-655.
57. Shahinpoor, M., *Conceptual design, kinematics and dynamics of swimming robotic structures using ionic polymeric gel muscles.* 1991.
58. Takagi, K., et al., *Development of a rajiform swimming robot using ionic polymer artificial muscles.* 2006 IEEE/RSJ International Conference on Intelligent Robots and Systems, Vols 1-12, 2006: p. 1861-1866.
59. Zheng Chen, J.Z., Tae I. Um, Hilary Bart-Smith. *Bio-inspired Robotic Cownose Ray Propelled by Electroactive Polymer Pectoral Fin*. in *ASME 2011 International Mechanical Engineering Congress & Exposition*. November 11-17, 2011. Denver, Colorado, USA.
60. Chen, Z., T.I. Um, and H. Bart-Smith, *Ionic Polymer-Metal Composite Enabled Robotic Manta Ray.* Electroactive Polymer Actuators and Devices (Eapad) 2011, 2011. **7976**.
61. Wang, Z.L., et al., *Embedded SMA wire actuated biomimetic fin: a module for biomimetic underwater propulsion.* Smart Materials & Structures, 2008. **17**(2).
62. Wang, Z.L., et al., *A micro biomimetic manta ray robot fish actuated by SMA.* 2009 Ieee International Conference on Robotics and Biomimetics (Robio 2009), Vols 1-4, 2009: p. 1809-1813.
63. Fukuda, T., Kawamoto, A., Arai, F., and Matsuura, H, *Mechanism and swimming experiment of micro mobile robot in water.* 1994.
64. Nagata, Y., et al., *Development of Underwater Robot using Macro Fiber Composite.* 2008 Ieee/Asme International Conference on Advanced Intelligent Mechatronics, Vols 1-3, 2008: p. 955-960.
65. Hirata, K. *Development of experimental fish robot*. in *ISME Tokyo 2000*. 2000.
66. Hirata, K., Takimoto, T., and Tamura, K. *Study on turning performance of a fish robot*. in *1st Int. Symp. Aqua Bio- Mechanisms*. 2000.
67. Fan, R.F., et al., *Optimized design and implementation of biomimetic robotic dolphin.* 2005 IEEE International Conference on Robotics and Biomimetics, 2006: p. 484-489.
68. Hu, H., *Biologically inspired design of autonomous robotic fish at Essex*, in *IEEE SMC UK-RI Chapter Conference*2006. p. pp. 3-8.
69. Shin, D., Na, S. Y., Kim, J. Y., and Baek, S. J., *Fish robots for water pollution monitoring using ubiquitous sensor networks with sonar localization*, in *2007 International Conference on Convergence Information Technology*2007. p. pp. 1298-1303.

70. Papadopoulos, E., E. Apostolopoulos, and P. Tsigkourakos, *Design, Control, and Experimental Performance of a Teleoperated Robotic Fish.* Med: 2009 17th Mediterranean Conference on Control & Automation, Vols 1-3, 2009: p. 766-771.
71. Wang, W.B., et al., *Bio-inspired Design and Realization of a Novel Multimode Amphibious Robot.* 2009 Ieee International Conference on Automation and Logistics (Ical 2009), Vols 1-3, 2009: p. 140-145.
72. Low, K. *Current and future trends of biologically inspired underwater vehicles*. in *Proc. of Defense Science Research Conference and Expo*. 2011.
73. Chen, Z., Um, T. I., Zhu, J. *Bio-inspired Robotic Cownose Ray Propelled by Electroactive Polymer Pectoral Fin*. in *ASME 2011 International Mechanical Engineering Congress & Exposition*. 2011.
74. Ding, R., et al., *CPG-based Dynamics Modeling and Simulation for a Biomimetic Amphibious Robot.* 2009 Ieee International Conference on Robotics and Biomimetics (Robio 2009), Vols 1-4, 2009: p. 1657-1662.
75. Hirata, K. *Development of experimental fish robot*. in *ISME Tokyo*. 2000.
76. Hirata, K., Takimoto, T., and Tamura, K. *Study on turning performance of a fish robot*. in *Proc. 1st Int. Symp. Aqua Bio- Mechanisms*. 2000.
77. Liu, J.D.a.H., H, *Biologically inspired behaviour design for autonomous robotic fish.* International Journal of Automation and Computing, 2006. **Vol. 3, No. 4, pp. 336-347**.
78. Hu, H., *Biologically inspired design of autonomous robotic fish at Essex*, in *IEEE SMC UK-RI Chapter Conference*2006. p. pp. 3-8.
79. Low, K. *Current and future trends of biologically inspired underwater vehicles*. in *Proc. of Defense Science Research Conference and Expo (DSR)*. 2011.
80. Low, K.H. and C.W. Chong, *Parametric study of the swimming performance of a fish robot propelled by a flexible caudal fin.* Bioinspiration & Biomimetics, 2010. **5**(4).
81. Shin, D., Na, S. Y., Kim, J. Y., and Baek, S. J., *Fish robots for water pollution monitoring using ubiquitous sensor networks with sonar localization*, in *International Conference on Convergence Information Technology*2007. p. pp. 1298-1303.
82. Shin, D., et al., *Fuzzy neural networks for obstacle pattern recognition and collision avoidance of fish robots.* Soft Computing, 2008. **12**(7): p. 715-720.
83. Uchino, K., *Piezoelectric actuators 2006 - Expansion from IT/robotics to ecological/energy applications.* Journal of Electroceramics, 2008. **20**(3-4): p. 301-311.
84. Cook-Chennault, K.A., N. Thambi, and A.M. Sastry, *Powering MEMS portable devices - a review of non-regenerative and regenerative power supply systems with special emphasis on piezoelectric energy harvesting systems.* Smart Materials & Structures, 2008. **17**(4).
85. Erturk, S., K.G. Seker, and M. Kosar, *Antioxidant Properties and Phenolic Composition of Alchemilla mollis from Turkey.* Planta Medica, 2011. **77**(12): p. 1383-1384.
86. Trolier-McKinstry, S. and P. Muralt, *Thin film piezoelectrics for MEMS.* Journal of Electroceramics, 2004. **12**(1-2): p. 7-17.
87. Meirovitch, L., *Fundamentals of vibrations*2001, Boston: McGraw-Hill. xviii, 806 p.
88. Wolf, K. and O. Gottlieb, *Nonlinear dynamics of a noncontacting atomic force microscope cantilever actuated by a piezoelectric layer.* Journal of Applied Physics, 2002. **91**(7): p. 4701-4709.
89. Usher, T. and A. Sim, *Nonlinear dynamics of piezoelectric high displacement actuators in cantilever mode.* Journal of Applied Physics, 2005. **98**(6).
90. Stanton, S.C., et al., *Nonlinear nonconservative behavior and modeling of piezoelectric energy harvesters including proof mass effects.* Journal of Intelligent Material Systems and Structures, 2012. **23**(2): p. 183-199.
91. Brunetto, P., et al., *A model of ionic polymer-metal composite actuators in underwater operations.* Smart Materials & Structures, 2008. **17**(2).
92. Maali, A., et al., *Hydrodynamics of oscillating atomic force microscopy cantilevers in viscous fluids.* Journal of Applied Physics, 2005. **97**(7).
93. Aureli, M., M.E. Basaran, and M. Porfiri, *Nonlinear finite amplitude vibrations of sharp-edged beams in viscous fluids.* Journal of Sound and Vibration, 2012. **331**(7): p. 1624-1654.
94. Aureli, M. and M. Porfiri, *Low frequency and large amplitude oscillations of cantilevers in viscous fluids.* Applied Physics Letters, 2010. **96**(16).

95. Lauder, G.V., *Hydrodynamics of undulatory propulsion.* 2005.
96. Taylor, G., *Analysis of the Swimming of Microscopic Organisms.* Proceedings of the Royal Society of London Series B-Biological Sciences, 1951. **139**(894): p. 141-141.
97. Taylor, G., *The Action of Waving Cylindrical Tails in Propelling Microscopic Organisms.* Proceedings of the Royal Society of London Series a-Mathematical and Physical Sciences, 1952. **211**(1105): p. 225-239.
98. Lighthil.Mj, *Large-Amplitude Elongated-Body Theory of Fish Locomotion.* Proceedings of the Royal Society of London Series B-Biological Sciences, 1971. **179**(1055): p. 125-&.
99. Taylor, G., *Analysis of the Swimming of Microscopic Organisms.* Proceedings of the Royal Society of London Series a-Mathematical and Physical Sciences, 1951. **209**(1099): p. 447-461.
100. Taylor, G., *Analysis of the Swimming of Long and Narrow Animals.* Proceedings of the Royal Society of London Series a-Mathematical and Physical Sciences, 1952. **214**(1117): p. 158-183.
101. Webb, P.W., and Weihs, D., *Fish Biomechanics*1983: Praeger Publishers, New York.
102. Lighthill, M.J., *Note on the Swimming of Slender Fish.* Journal of Fluid Mechanics, 1960. **9**(2): p. 305-317.
103. Abdelnour, K., et al., *Hydrodynamics of underwater propulsors based on ionic polymer-metal composites: a numerical study.* Smart Materials & Structures, 2009. **18**(8).
104. Anton, S.R., A. Erturk, and D.J. Inman, *Multifunctional self-charging structures using piezoceramics and thin-film batteries.* Smart Materials and Structures, 2010. **19**(11).
105. Lauder, G.V. and E.G. Drucker, *Forces, fishes, and fluids: hydrodynamic mechanisms of aquatic locomotion.* News in physiological sciences, 2002. **17**: p. 235-240.